

FLIGHT DYNAMIC SIMULATION MODELING OF LARGE FLEXIBLE TILTROTOR AIRCRAFT

Ondrej Juhasz Roberto Celi
 Doctoral Candidate Professor
 Department of Aerospace Engineering
 University of Maryland
 College Park, MD

Christina M. Ivler
 Aerospace Engineer
 Aeroflightdynamics Directorate (AMRDEC)
 U.S. Army Research, Development, and Engineering Command
 Moffett Field, CA

Mark B. Tischler
 Senior Scientist

Tom Berger
 Aerospace Engineer
 University Affiliated Research Center (UCSC)
 NASA Ames Research Center
 Moffett Field, CA, USA

A high-order rotorcraft mathematical model is developed and validated against the XV-15 and a Large Civil Tilt-Rotor (LCTR) concept. Rigid body and inflow states, as well as flexible wing and blade states are used in the analysis. The separate modeling of each rotorcraft component allows for structural flexibility to be included in the presented formulation, which is important when modeling large aircraft where structural modes effect the frequency range of interest for flight control, generally 1 to 20 rad/sec. Details of the formulation of the mathematical model are given, including derivation of structural, aerodynamic, and inertial loads. The linking of the components of the aircraft is developed using an approach similar to multibody analyses by exploiting a tree topology, but without equations of constraints. Assessments of the effects of wing flexibility are given. Flexibility effects are evaluated by looking at the nature of the couplings between rigid body modes and wing structural modes and vice versa. A model following control architecture is then implemented on full order LCTR models with and without structural flexibility. The rigid wing model is shown to give Level 1 handling qualities, whereas the wing flexible model exhibits poor handling qualities. Notch filters are introduced to eliminate wing structural dynamics from the output equations. The aircraft response with notch filters is shown to be much improved with respect to stability margins and handling qualities requirements for the LCTR.

Notation

Variables

a	Acceleration vector	q	Displacement vector, inertial moment vector
F	Modal forcing	r	Position vector
K	Linear stiffness matrix	S	Coordinate system transformation matrix
M	Linear mass matrix	v	Velocity vector
n	Unit vectors of a coordinate system, nodal displacement vector	v, w	Elastic displacements
N	Modal spatial displacement of a point	V	Modal matrix
p	Forcing vector	x_0	Displacement from start of elastic portion of beam
P	Position vector	y_0, z_0	Offsets from elastic axis to center of mass
p, q, r	Body angular rates	z	Partial fraction zero
		α	Aerodynamic angle of attack, rotation vector
		β	Aerodynamic sideslip angle
		η	Structural control or stability derivative
		δ	Pilot stick input (inches)
		ϕ, θ, ψ	Euler angles
		Φ	Influence coefficient

Presented at the American Helicopter Society 68th Annual Forum, Fort Worth, Texas, May 1-3, 2012. Copyright ©2012 by the authors except where noted. All rights reserved. Published by the AHS International with permission.

ω	Rotation rates, frequency
Ω	Skew symmetric matrix of rotation rates
ρ	Modal temporal displacement of a point
ψ	Azimuth angle
ζ	Offset from reference frame to first body

Subindices

<i>a</i>	Antisymmetric mode
<i>A</i>	Aerodynamic
<i>B</i>	Blade
<i>col</i>	Collective stick
<i>D</i>	Damping
<i>E</i>	External
<i>f</i>	Flexibility
<i>I</i>	Inertial
<i>lat</i>	Lateral cyclic stick
<i>lon</i>	Longitudinal cyclic stick
<i>ped</i>	Pedal
<i>rb</i>	Rigid-Body
<i>s</i>	Symmetric mode
<i>S</i>	Structural
<i>str</i>	Structural mode

Abbreviations

ACAH	Attitude Command Attitude Hold
CG	Center of Gravity
DAE	Differential-Algebraic Equation
HQ	Handling Qualities
LCTR	Large Civil Tilt-Rotor
MTE	Mission Task Elements
ODE	Ordinary Differential Equation
PIO	Pilot Induced Oscillations

Motivation

Tilt-rotor configurations have been proposed for both civil and military heavy-lift vertical take-off and landing (VTOL) missions. An in-depth NASA investigation examined several types of rotorcraft for large civil transport applications, and concluded that the tilt-rotor had the best potential to meet the desired technology goals. It also presented the lowest developmental risk of the configurations analyzed (Ref. 1). One of the four highest risk areas identified by the investigation was the need for broad spectrum active control, including flight control systems, rotor load limiting, and vibration and noise reduction (Ref. 1).

The development of a high-order model is paramount for accurately predicting a wide range of stability phenomena that tilt-rotors are susceptible to, and is the main subject of this paper. The best known aeromechanic stability problem for tilt-rotor aircraft is whirl-flutter, which occurs at high advance ratios, and usually limits forward flight speed. At hover and low speeds, pilot inputs can excite low frequency wing structural modes for large tilt-rotor configurations like the Large Civil Tilt-Rotor (LCTR), Fig. 1. Lateral stick inputs, for example, result in anti-symmetric wing bending

motion. This wing structural response can cause low stability margins if the dynamics are not accounted for in flight control design. The structural modes for future large tilt rotors are likely to be in the range of interest for control system design, around 1/3 to 3 times the response crossover frequency, generally 1 to 20 rad/sec. Most rotorcraft also tend to have increased levels of augmentation compared to fixed-wing aircraft, especially in hover and low speed where precision flying is necessary. Clearly, the success of these configurations will require an improved fundamental understanding of the interactions between handling qualities, high-gain flight control systems, and aircraft structural dynamics.

Prior Work

One of the first experimental tilt-rotor aircraft, the XV-15, was developed in the 1970's and 1980's. To support analysis of flight dynamics, pilot-in-the-loop simulation, and flight control, the Generic Tilt-Rotor Simulation (GTRSIM) was developed (Ref. 2). GTRSIM is based heavily on wind tunnel data from the XV-15 in the form of lookup tables to augment the rigid body dynamics. The detailed lookup tables include effects of nacelle angle, sideslip, flap deflections, Mach number, etc., on aerodynamic coefficients and contain correction factors to the dynamic response of the aircraft.

Later, CAMRAD, a comprehensive aeromechanics and dynamics model capable of multi-rotor and flexible airframe modeling (Ref. 3), was used to model the heavy lift helicopters that are of interest herein. CAMRAD was later updated to CAMRAD II and offers a larger suite of analysis tools, and has been used extensively for tilt-rotor development and analysis (Refs. 4, 5). These analyses focused on optimization of the large civil tilt rotor for performance and whirl-flutter. Performance optimization included rotor sizing and geometry as well as cruise tip speeds. Whirl-flutter optimization included cruise tip speeds, precone and other rotor metrics.

Although CAMRAD is not a real-time tool, linear models derived from CAMRAD were used in NASA's Vertical Motion Simulator in piloted simulations (Refs. 7–10) designed to test hover and low speed handling qualities and control system architectures of the LCTR. These models were based on a combination of reduced-order stability derivative models and more detailed rigid-body models that included rotor flapping dynamics, but lacked structural flexibility. Despite these limitations, the linear rigid body model was sufficient for determining handling qualities characteristics of large tilt-rotors. The key findings included: (i) the need to loosen the requirements for ADS-33E mission task elements as appropriate to the large vehicle configuration; (ii) that the large CG to pilot station offset resulted in lateral accelerations that were unfavorable to the pilot with traditional yaw bandwidth requirements,

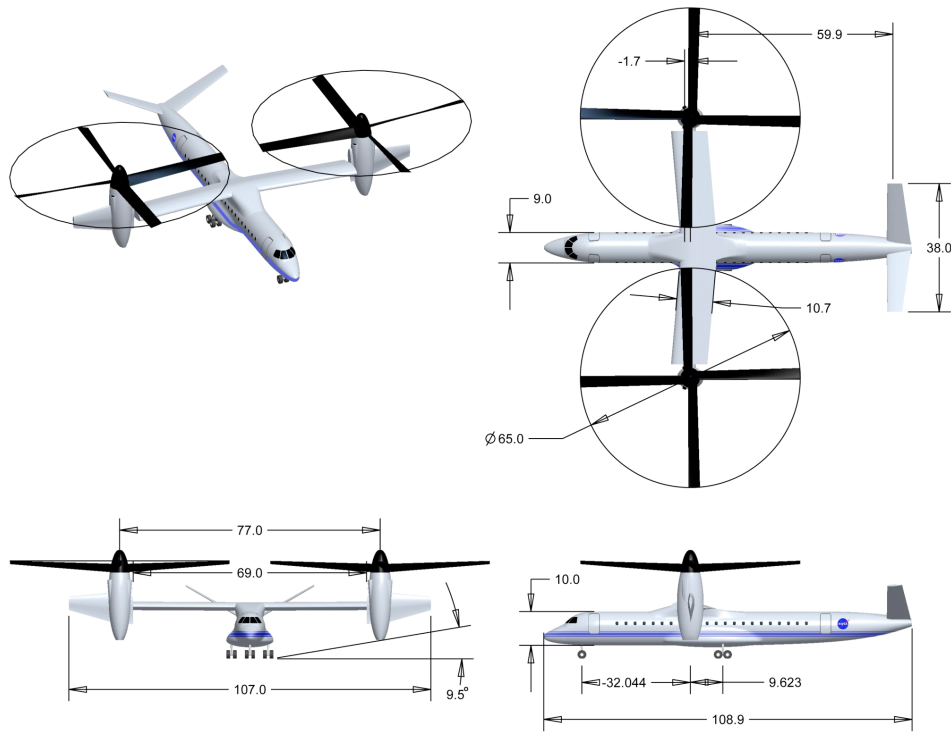


Fig. 1. Configuration and dimensions of the NASA Large Civil Tiltrotor (LCTR) (from Ref. 4).

therefore, a modified yaw bandwidth criteria was proposed; and (iii) that increased disturbance rejection characteristics with relaxed stability margins were found to yield more favorable piloted handling qualities (Ref. 7).

First-principles, nonlinear real-time models that include rotor and body flexibility will be needed for more advanced investigations.

The model used in this work, and referred to as Helium 2, has been in development at the University of Maryland for many years and is a successor to the model first mentioned in Ref. 11. It originated from the NASA version of GenHel, built from a mathematical model by Howlett (Ref. 12), and over time has evolved to include flexible rotors and free-vortex wake models. More recently, the code has been augmented to include multi-rotor capabilities. The current research effort has expanded this to include flexible wings and an overall multibody-like formulation. The model is generic and allows for any rotorcraft configuration, from single main rotor helicopters to coaxial and tilt-rotor aircraft. Fuselage and wing aerodynamics portions of GTRSIM were added to this model. The model was therefore validated against the XV-15 before being scaled to the LCTR configuration.

Objectives

The main objectives of this paper are:

1. To present the development and validation of a high fidelity flight dynamics model applied to flexible tiltrotor configurations. The mathematical model is first developed. Details are given regarding the formulation of the problem including kinematic and coordinate system considerations. Structural, inertial, and aerodynamic components of a beam model are also extended to be used for tilt-rotor wings. Specifically, downwash and tip masses are accounted for. Validation is first performed against XV-15 tilt-rotor aircraft flight test data, with a rigid wing model only. The model is then extended to the LCTR. The flexible wing model is then compared to a rigid wing model using frequency response analysis.
2. To study the influence of high-order rotor and structural flexibility on the dynamics of large tilt-rotors through reduced order models.
3. To discuss the effects of aeroelastic coupling and rigid-body coupling on the reduced order models of the LCTR. The models are reduced to only include rigid-body and wing structural states. Aeroelastic coupling refers to the effect of wing flexibility on rigid body

states and rigid-body coupling refers to the effect of rigid-body states on the flexible wing. Reduced order uncoupled models simplify the model structure needed for system identification, but must remain valid over the frequency range of interest.

4. To describe the development of model following control laws for three levels of modeling fidelity. The baseline model considered first is a rigid wing model. Next, wing flexibility is introduced and optimization results in a new set of gains. Finally, notch filters are used on the state feedback and feedforward paths in the roll, pitch, and yaw axes to suppress wing excitation.

Theoretical Development

A description of the formulation of the equations of motion, specifically for the wing is given in this section. Along with the beam equations, consideration of the effects of wing flexibility are also discussed. Structural flexibility effects the kinematics of all bodies upstream of the current one, and a “quasi multibody” formulation is used in the formulation described to connect the bodies. A full multibody formulation is generally characterized by:

1. *Numerical kinematics* — Position vectors, velocities, and accelerations are all built numerically, with no algebraic manipulations, ordering schemes, or limitations on magnitude of displacements and rotations. Furthermore, the kinematic formulation can be extended in an automated way to any number of bodies in a chain.
2. *Enforcement of connectivity through explicit equations of constraint* — The equations are generally algebraic, resulting in an overall model that is formulated as a system of Differential Algebraic Equations (DAEs) rather than a system of Ordinary Differential Equations (ODEs).

The present model implements numerical kinematics, but does not include explicit equations of constraint.

The lack of explicit constraint equations makes the model less flexible than full multibody formulations. The topology is limited to tree-like arrangements without loops, and connectivity that cannot be described by adding or removing nodal degrees of freedom requires changes to the software implementation. Moreover, the formulation is less suitable for software interfaces in which users assemble the model from point-and-click selections of element libraries.

On the other hand, the model naturally results in a system of ODEs, modal coordinate transformations are easily implemented, and there is no need to solve DAE systems (typically of index 3 or higher) or use techniques to condense out algebraic equations of constraints or convert them to ODEs. If necessary, equations of constraints

could simply be added to the present formulation through the use of Lagrange multipliers and suitable DAE solvers. All structural and inertia couplings are rigorously modeled. The aerodynamic couplings need to be analyzed on a configuration-by-configuration basis, and may require additional configuration-specific modeling, but this is also true for full multibody formulations. Because the present formulation allows for an arbitrary number of rotors of arbitrary position and orientation, and any number of flexible aerodynamic surfaces located anywhere on the aircraft, it is still sufficiently general to formulate flight dynamic models for all configurations envisioned for future rotorcraft with little or no recoding.

The model is formulated as a series of nested loops (from outermost to innermost: over rotors, blades or wings, finite elements, and Gauss points within elements), uses modal coordinate transformations, and contains no coupled algebraic equations. With the exception of the blade inertia load calculations (because of the centrifugal force), all loops can be traversed in any order, and can be easily parallelized. As a result, real-time execution is achievable on off-the-shelf workstations with no approximations for models of realistic complexity. Software granularity is also sufficient for CUDA/GPU-based real time implementations.

Details of the baseline blade equations of motion can be found in Ref. 13, and serve as a starting point for the discussion regarding the wing equations. The equations of motion can be broken down into three key components; inertial, structural, and aerodynamic loads.

Kinematics and Coordinate System Transformations

The rotorcraft model consists of multiple flexible bodies arranged in a generic tree-like topology. For the tilt-rotor examples of the present study, shown in Fig. 2, the tree starts from the aircraft center of mass and branches out to the wings, pylons, and ultimately rotors and blades. Each component within this tree is given its own coordinate system. The coordinate system serves as the basis for the formulation of flexibility contributions of that body to the overall system. The local coordinate system for the wing has the same sign conventions as those of the elastic blade.

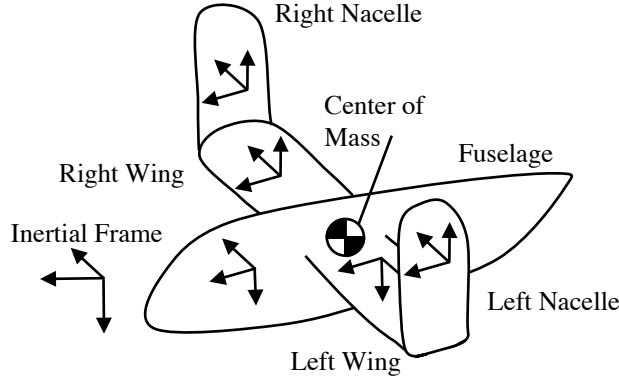


Fig. 2. Generic tilt-rotor multi body formulation

The development of the kinematic relations between the bodies is given in the Appendix and covers derivations of the positions, velocities, and accelerations of arbitrary points within the tree-like configuration.

Beam Element Description

The model is entirely composed of a coupled set of nonlinear ODEs, and modal coordinate transformations are used. Blade and wing mode shapes are calculated at the beginning of each simulation or can be read from files. Mode shapes for the wing assume cantilever connections to an immovable object. In the dynamic system, wing motion produces forces and moments on the fuselage causing coupled motion.

Beam finite elements are used to model the blades, with coupled torsion and flap-lag bending degrees of freedom, and small elastic deflections. Four elements are used to model each wing and blades. Aerodynamic, structural, and inertial forces and moments are calculated at specified internal points in each finite element, integrated to form nodal loads, and finally transformed into modal loads, greatly reducing the total number of degrees of freedom. All loads are formed in the undeformed beam coordinate system. This makes force and moment contributions to the body downstream of the elastic body easier to calculate. The same finite element is used to model the wings. A finite state wake inflow model is used for each rotor.

Inertia and structural couplings are rigorously modeled for any combination of rotors and wings. The aerodynamic couplings need to be tailored for every specific configuration. For the XV-15 model in the present study, the airframe aerodynamics, including impingement of the downwash on the wing surfaces, and inflow effects on the elevator and rudders, are modeled using the flight test-derived data tables in Ref. 2. For the hover LCTR case, only downwash impingement on the wing is modeled. Aerodynamic contributions from the empennage are neglected.

A thorough discussion of the elastic blade formulation can be found in Ref. 13. The following discussion high-

lights the contributions from tip masses and large external objects, like the nacelle, on the beam equations.

Inertial Loads: The LCTR uses a tip mass to decrease hover coning and thus increase figure of merit (Ref. 1). The tip mass is assumed to be a point load on the beam elastic axis. It is located at the 95% radial location of the blade. The nacelle is assumed to be a mass centered at a distance $y_0 \mathbf{n}_2^k + z_0 \mathbf{n}_3^k$ from the elastic axis. The y_0 and z_0 displacements are in the deformed beam coordinate system. This formulation retains the built in displacements assumed for the elastic blade. The generic position for a point on the blade in the undeformed blade coordinate system is:

$$\mathbf{r}_B = \begin{bmatrix} e \cos \beta_p + x_0 + S_{21}^{kj} y_0 + S_{31}^{kj} z_0 \\ v + S_{22}^{kj} y_0 + S_{32}^{kj} z_0 \\ w - \sin \beta_p + S_{23}^{kj} y_0 + S_{33}^{kj} z_0 \end{bmatrix} \mathbf{n}_1^j + \quad (1)$$

The transformation matrix $[S]$ transforms the offsets from the deformed to the undeformed coordinate system. Its components are given by Eqn. (A.5). v and w are elastic contributions to the displacement of the elastic axis. e is the offset from the beam connection point to the start of the elastic portion of the beam. β_p is the precone angle. The displacement is written in general terms as:

$$\mathbf{r}_B = r_x \mathbf{n}_1^j + r_y \mathbf{n}_2^j + r_z \mathbf{n}_3^j \quad (2)$$

with

$$\begin{aligned} r_x &= r_{11} + r_{12}x_0 + r_{13}y_0 + r_{14}z_0 \\ r_y &= r_{21} + r_{22}x_0 + r_{23}y_0 + r_{24}z_0 \\ r_z &= r_{31} + r_{32}x_0 + r_{33}y_0 + r_{34}z_0 \end{aligned}$$

Inertial loads are based on finding the absolute acceleration of a mass. As with the position vector, Eqn. (1), the beam acceleration vector retains a generic formulation where offsets from the elastic axis are retained. The full acceleration vector in the undeformed coordinate system is given as:

$$\mathbf{a}_B = a_x \mathbf{n}_1^j + a_y \mathbf{n}_2^j + a_z \mathbf{n}_3^j \quad (3)$$

with

$$\begin{aligned} a_x &= a_{11} + a_{12}x_0 + a_{13}y_0 + a_{14}z_0 \\ a_y &= a_{21} + a_{22}x_0 + a_{23}y_0 + a_{24}z_0 \\ a_z &= a_{31} + a_{32}x_0 + a_{33}y_0 + a_{34}z_0 \end{aligned}$$

The first terms, a_{11} , a_{21} , and a_{31} contain all rigid body and flexibility acceleration contributions up to the shaft. These accelerations also contain acceleration terms specific to the elastic rotor blade that do not depend on offsets from the elastic axis. Once the acceleration of the point is known, the inertial forces follow.

$$\mathbf{p}_I = -m \mathbf{a}_B \quad (4)$$

Displacements from the deformed coordinate system to the center of mass of the blade or tip element in the chordwise and vertical directions, n_2^k and n_3^k , respectively, create moments at the blade section.

$$\mathbf{q}_I = -m \left[(y_0 \mathbf{n}_2^k + z_0 \mathbf{n}_3^k) \times \mathbf{a}_B \right] \quad (5)$$

The full moment vector is:

$$\mathbf{q}_I = -m \left[M_1 \mathbf{n}_1^j + M_2 \mathbf{n}_2^j + M_3 \mathbf{n}_3^j \right] \quad (6)$$

with

$$\begin{aligned} M_1 &= q_{13}y_0 + q_{14}z_0 + q_{15}x_0y_0 + q_{16}x_0z_0 + q_{17}y_0z_0 \\ &\quad + q_{18}y_0^2 + q_{19}z_0^2 \\ M_2 &= q_{23}y_0 + q_{24}z_0 + q_{25}x_0y_0 + q_{26}x_0z_0 + q_{27}y_0z_0 \\ &\quad + q_{28}y_0^2 + q_{29}z_0^2 \\ M_3 &= q_{33}y_0 + q_{34}z_0 + q_{35}x_0y_0 + q_{36}x_0z_0 + q_{37}y_0z_0 \\ &\quad + q_{38}y_0^2 + q_{39}z_0^2 \end{aligned}$$

The quantities q above contain products of the components of the position and acceleration vectors. The tip mass does not create moments at the cross section since it is located on the elastic axis. The nacelle's moments of inertia are lumped into two radii of gyration, one along y_0 and the other along z_0 . The nacelle is assumed to be a cylinder of constant mass distribution. The parallel axis theorem is used to derive the radius of gyration with respect to the connection point to the wing, which is below the center of mass. Due to the symmetry of the pylon, mass products of inertia are generally zero.

Once the section forces and moments are known, they are integrated into the nodal forces for the given finite element.

Structural Loads: The structural load equations for the elastic wings do not differ from those of the elastic blades. Wing stiffness information was derived to produce the same fundamental wing frequencies as given in Ref. 4. The current study focuses on hover dynamics, specifically in the lateral/directional axes. It was therefore important to match wing antisymmetric beamwise and chordwise bending modes. The mode shapes of the elastic beams generally contain coupled beamwise, chordwise, and torsion bending. The mode is named after the dominant response. Therefore, a beamwise mode will contain mostly beamwise bending but could also contain chordwise and torsion bending. Figure 3 shows the beam modes and nomenclature used in this analysis. The motion of the left and right wing are independent in the formulation and therefore symmetric and asymmetric modes are not explicitly formed. The following coordinate transformation is used to transform from the independent wing degrees of freedom to symmetric and asymmetric degrees of freedom.

$$\begin{Bmatrix} \mathbf{q}_1 \\ \mathbf{q}_2 \end{Bmatrix} = \begin{bmatrix} 1 & 1 \\ 1 & -1 \end{bmatrix} \begin{Bmatrix} \mathbf{q}_s \\ \mathbf{q}_a \end{Bmatrix} \quad (7)$$

\mathbf{q}_1 and \mathbf{q}_2 are the modal deflections of the left and right wing and \mathbf{q}_a and \mathbf{q}_s are the same deflections given in terms of antisymmetric and symmetric modes.

Aerodynamic Loads: The aerodynamic forcing is again formulated in essentially the same manner as the elastic blade. The wing is approximately 1/3 R below the main rotor and is assumed to be immersed in the wake of the rotor. The components of the inflow velocity are obtained from the dynamic inflow coefficients of the rotor at the 270 deg azimuth position, approximately the azimuth position of blade passage over the wing. These inflow velocities are then augmented by the nacelle angle to find the local velocity at the wing section. The same wing airfoil data is used for the LCTR as was available for the XV-15. This airfoil data includes aerodynamic coefficients for very large angles of attack as are needed by a wing experiencing downwash in hover. The XV-15 aerodynamic coefficient look up tables are functions of angle of attack, mach number, nacelle angle, and flap setting. For the LCTR hover case, the portions of the look up tables with the nacelle in the vertical position and flaps retracted were used. The total download as a fraction of gross weight in hover was similar to that of the XV-15 in hover.

Model Development and Validation

This section discusses in more depth the formulation of the quasi-multibody tilt-rotor model and includes validation results against the XV-15.

Tree Structure Management

At each time step, the only information each individual body has is that of the connection to the bodies just upstream of itself. This information contains the displacement vector \mathbf{q} to the connection point of that body, and the set of rotations needed to get to the coordinate system of the next body. This allows for components of the system to be easily swapped out with other components with minimal changes to the inputs. Information regarding each body is stored individually with that body in derived types, allowing for large systems to be constructed with minimal creation of vectors that must be passed through each subroutine. A tree array is formed to join the system of individual bodies into the full multibody system of the aircraft and contains pointers to each of the derived types. A tree array for a generic set of interconnected bodies, shown in Fig. 4, is given in Table 1. The top line of the table contains a numerical assignment for each body in the system. The columns of the table indicate the path from that body to the reference frame. For the tilt rotor example, the fuselage, wings, and nacelles each have their own derived type. A tree array is formed and assigns body numbers to each component of the aircraft. Since some components are used twice, some

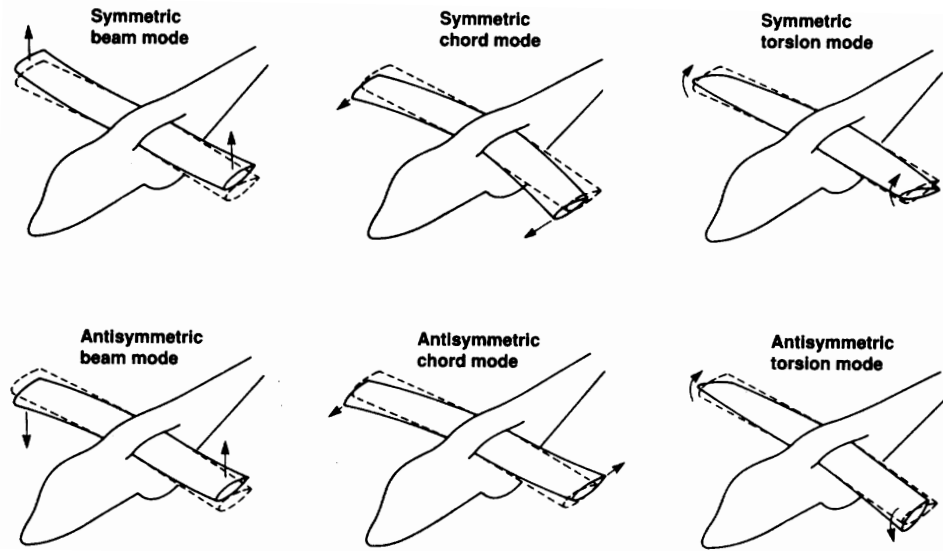


Fig. 3. Tilt-rotor beam mode shapes (Ref. 6)

body numbers are composed of the same derived type. As the kinematics of the system are created, the appropriate body is extracted from the set of all available bodies using the tree array.

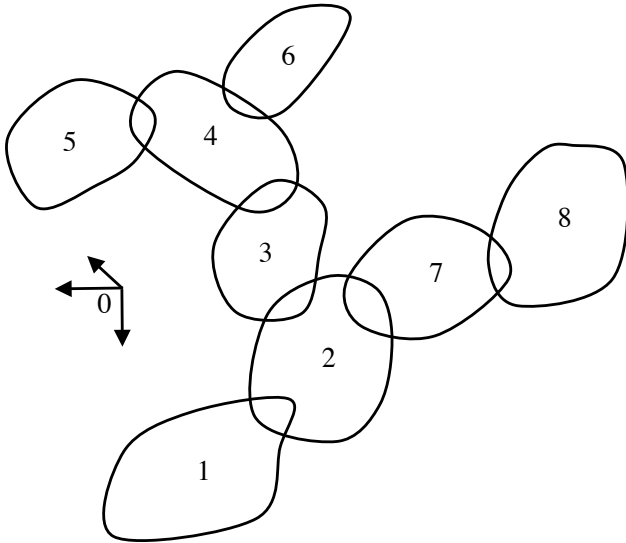


Fig. 4. Generic set of interconnected bodies

k	1	2	3	4	5	6	7	8
Γ_1	0	1	2	3	4	4	2	7
Γ_2		0	1	2	3	3	1	2
Γ_3			0	1	2	2	0	1
Γ_4				0	1	1		0
Γ_5					0	0		

Table 1. Tree array connecting the components of Fig. 4

The formulation of all components of the tree structure, including the coordinate system transformation matrices, kinematic relations, and kinematic vector transformations

are done in unison in loops based on the length of each branch of the tree. All loops begin at the reference frame and branch out depending on the number of connections each individual body has. To obtain the kinematics of the final body in the tree system, the kinematic relations of all other bodies downstream of that one must be created first. This formulation reduces the number of matrix multiplications needed to model the entire system.

Modal Analysis

Blade and wing modal analysis is used to reduce the overall degrees of freedom of the system. Full mass and stiffness matrices for each wing or blade are only formulated once at the beginning of execution. The mass matrix is obtained from a central difference approximation to perturbations of the second time derivative of the nodal degrees of freedom. The stiffness matrix comes from a central difference approximation to perturbations in displacement of the nodal degrees of freedom. The matrices are approximations because the beam equations are generally nonlinear. The linear matrices can be written as:

$$[\mathbf{M}] \ddot{\mathbf{n}} + [\mathbf{K}] \mathbf{n} = 0 \quad (8)$$

The blade modes are obtained in a vacuum, i.e. aerodynamic loads are not included. There are a total of $6N_E + 5$ nodal degrees of freedom, where N_E is the total number of finite elements used in the formulation. The nodal degrees of freedom for each finite element are displacement and slope for flap (w) and lag (v) motions at the inboard and outboard end of each element. Torsion (ϕ) has degrees of freedom at the inboard and outboard end, as well as at the center of each element, as shown in Fig. 5.

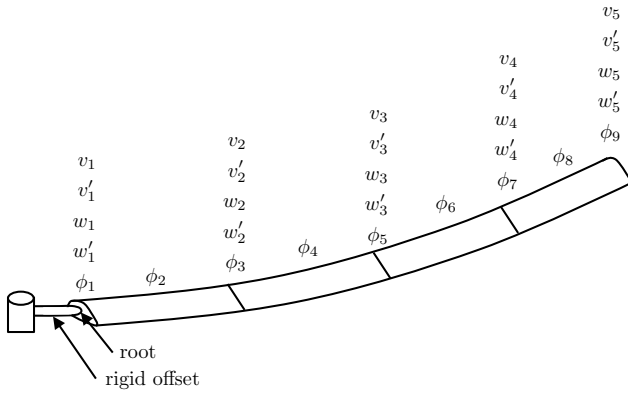


Fig. 5. Four element finite element model of a blade with nodal degrees of freedom

Eigen analysis produces a matrix of mode shapes, $[\mathbf{V}]$, which consists of columns of eigenvectors, along with a vector of the square of the corresponding modal frequencies, $\{\omega^2\}$, such that:

$$-\omega_i^2 [\mathbf{M}] \{\mathbf{v}_i\} + [\mathbf{K}] \{\mathbf{v}_i\} = 0 \quad (9)$$

Here, \mathbf{v}_i is the eigenvector associated with mode i . Each column in the matrix of mode shapes gives the modal displacements for the mode associated with that column. Four finite elements are used for the formulation of each blade and wing. The maximum number of modes retained is therefore 29, however, only the two lowest frequency modes are retained for each wing and blade since the dominant response of the system comes from the low frequency modes. Higher frequency modes do little to alter the dynamics in the frequency range of interest. For example, the third wing mode occurs around 40 rad/sec and is not retained in the current analysis. Modal reduction reduces the overall degrees of freedom of the system. The total nodal displacement can be written as the product of the columns of the $[\mathbf{V}]$ matrix associated with retained modal displacements \mathbf{q} :

$$\mathbf{n} = [\mathbf{V}] \mathbf{q} \quad (10)$$

Throughout the remainder of execution, blade and wing motion are limited to summed contributions from the retained modes. This summed contribution goes into determining the displacement and angles that flexibility add to the kinematics of the multibody system, given in Eqn. (A.10).

The distributed forces on each finite element are integrated across the element to produce nodal loads. The nodal loads are reduced to modal loads using the transpose of the transformations that produces nodal degrees of freedom from modal degrees of freedom. For example,

$$\mathbf{F}_I = [\mathbf{V}]^T \mathbf{p}_I \quad (11)$$

Here, \mathbf{F}_I are the modal inertial load and \mathbf{p}_I are nodal loads.

The sum of the modal inertial, aerodynamic, and structural loads produce the equilibrium equation for that mode.

Artificial damping was added to the wing equations to produce stable modes with 4% damping ratios. The majority of the flexible bodies in the system are connected to other bodies which also produce forces and moments at the connection point to the current body. These external forces and moments are also reduced to modal forcing. In equilibrium, the blade modal equations can be written as:

$$\mathbf{F}_I + \mathbf{F}_A + \mathbf{F}_S + \mathbf{F}_D + \mathbf{F}_E = \mathbf{0} \quad (12)$$

Trim

The trim solution defines an equilibrium point for the aircraft for a given flight condition, and is produced by the solutions of algebraic equations. The aircraft can be trimmed for forward speeds, as well as steady coordinated climbing turns. The equations of motion for the aircraft are written as first order ordinary differential equations, and the trim conditions and unknowns must be able to uniquely define all the states of the system. The following are the trim conditions: V , total aircraft velocity; ψ , turn rate; and γ , flight path angle. Except for parts of the XV-15 validation, the work presented here consists entirely of the hover condition.

The rigid body trim unknowns are as follows:

$$\{\delta_{lat} \delta_{lon} \delta_{col} \delta_{ped} \alpha \beta \phi \theta\} \quad (13)$$

The first four unknowns are the pilot stick inputs. α and β are angles of attack and sideslip of the fuselage, respectively. ϕ and θ are roll and pitch Euler angles. The trim conditions and unknowns produce an overall equilibrium in aircraft forces and moments. They also ensure turn coordination and adherence to the flight path angle equation. The rigid body equations are integrated around the azimuth to ensure a trim state for a full rotor revolution.

The blade equations of motion are second order in time. To convert the differential blade equations into algebraic equations, blade periodicity is assumed around the azimuth. Each blade mode is allowed to have a constant component of motion around the azimuth as well as three harmonics. The trimmed modal equations have the following form:

$$\mathbf{q} = \mathbf{q}_0 + \sum_{i=1}^{N_h} (\mathbf{q}_{ic} \cos i\psi + \mathbf{q}_{is} \sin i\psi) \quad (14)$$

The above equation can be easily differentiated twice to produce the needed modal velocities and accelerations. The unknowns in the trim algebraic solution are the steady state and harmonic coefficients. For the current simulations, $N_h = 3$ harmonics are retained, so a total of 7 unknowns exist for each blade mode. The equilibrium equations for the blades are also integrated around the azimuth. They are based on the Galerkin method of residuals. Generally Eqn. (12) is not equal to 0, but rather a residual that is dependent on the current azimuth position, $res(\psi)$. From

Eqn. (14), there are $2N_h + 1$ unknowns, so $2N_h + 1$ trim equations are needed. The trim equations for the blade modal unknowns aim to minimize this residual and its harmonics as follow.

$$\begin{aligned} \int_0^{2\pi} res(\psi) d\psi &= 0 \\ \int_0^{2\pi} res(\psi) \cos i\psi d\psi &= 0 \quad i = 1, \dots, N_h \\ \int_0^{2\pi} res(\psi) \sin i\psi d\psi &= 0 \quad i = 1, \dots, N_h \end{aligned} \quad (15)$$

The flexible wing equations of motion are of the same form as the blade. In trim, the wings are only allowed constant deflections, so the trim unknowns become:

$$\mathbf{q} = \mathbf{q}_0 \quad (16)$$

Since there is only one unknown per wing mode, each wing mode only has one associated trim equation.

Dynamic inflow trim equations and unknowns are also used in the analysis. Each rotor has a constant coefficient and first harmonic sine and cosine inflow distribution. The dynamic inflow equations are written in first order ODE form. In trim the time derivative of the inflow equations must be zero when integrated around the azimuth.

Linearization

The full aircraft nonlinear equations are written in first order form. Linearization is obtained from taking a Fourier series approximation to the nonlinear equations of motion and truncating the approximation at the first derivative, leaving a steady state term and a linear derivative term. The steady state term describes the trim condition and is generally used as the basis for the perturbations. A central difference scheme is used for the first derivative. Perturbations of the time derivative of the state vector produce a mass matrix which is dependent on the current azimuth, $E(\psi)$. Perturbations to the state vector produce a matrix of stability derivatives, $F(\psi)$. Perturbations to the control vector produce control derivatives, $G(\psi)$, such that:

$$E(\psi)\dot{x}(\psi) = F(\psi)x(\psi) + G(\psi)u(\psi) \quad (17)$$

or

$$\dot{x}(\psi) = \underbrace{E(\psi)^{-1}F(\psi)}_{A(\psi)}x(\psi) + \underbrace{E(\psi)^{-1}G(\psi)}_{B(\psi)}u(\psi) \quad (18)$$

The $A(\psi)$ and $B(\psi)$ matrices are functions of azimuth, and generally the average of these is taken around a rotor revolution to obtain a constant coefficient system. These averaged A and B matrices are used for validation and the subsequent analyses presented in this paper.

Free Flight Response

Starting from a set of initial conditions, the equations of motion can be integrated in time to form a free flight response of the aircraft. Generally a trimmed solution is used as the set of initial conditions and step or impulse commands can be given for stability analysis in the time domain.

Validation with XV-15

An important first step was to validate the model against flight data for a known configuration to test its fidelity. The model was validated against the XV-15 before being applied to the LCTR. The XV-15 was chosen because simulation input data, such as aerodynamic tables, and flight responses that can be used for validation were readily available in the public domain. XV-15 input data were obtained from the GTRSIM manual and sample code inputs. Blade structural data was not a part of the GTRSIM simulations and was derived from a UH-60 blade input block. Only the first structural mode was retained for the blade, which was a rigid body flapping mode, meaning the blade structure contributions to the blade equations of motion remained unexcited.

Hover Figure 6 shows a frequency response comparison of the XV-15 roll rate to lateral stick inputs in hover. The curve labeled ‘‘HeliUM’’ represents the model developed in the present study. The curve marked ‘‘ID Model’’ comes from a state space model derived from flight test data using system identification. The ‘‘GTRSIM’’ model represents a state space model derived from the GTRSIM software. Stability and control derivatives for both comparison curves can be found in Ref. 16. ‘‘Flight Data’’ curves are derived from frequency sweeps performed during test flights. The roll response is measured in rad/sec, while the input is degrees of aileron deflection. Control surface deflections are downstream of the stability and control augmentation systems and are geared with swashplate inputs. They are used to measure the input for the bare airframe responses. The roll response curve is dominated by the low frequency lateral phugoid mode. Overall, there is good agreement between the HeliUM curve and the GTRSIM and ID models. While the unstable phugoid frequency agrees well with flight test data, there is a 5 dB over prediction of the roll response by the models as compared to flight data.

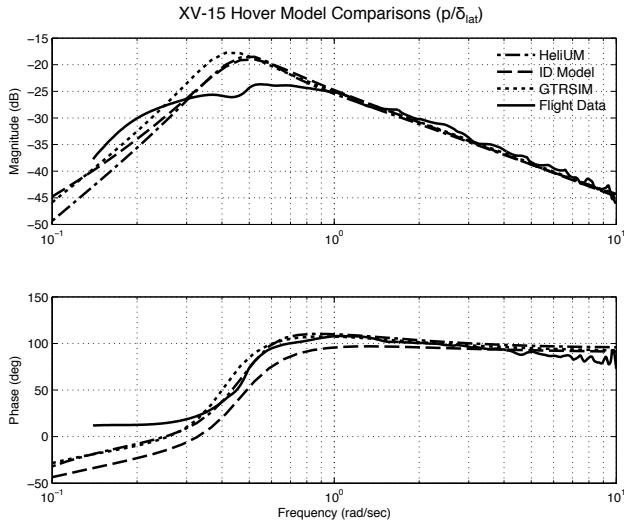


Fig. 6. XV-15 hover roll rate response to lateral stick inputs.

The hover yaw rate response is shown in Fig. 7. Here, the units are rad/sec of yaw rate for input degrees of rudder deflection, which is geared with antisymmetric longitudinal swashplate inputs. The yaw response is essentially a first order system that has a pole at low frequency, giving a constant -20 db/dec slope at the frequencies shown in the figure. The offset in the HeliUM magnitude response above 0.6 rad/sec can be attributed to the modeling of the hub. The XV-15 has a gimbaled hub, while the present model has an articulated hub, with the gimbal behavior approximated through flapping springs.

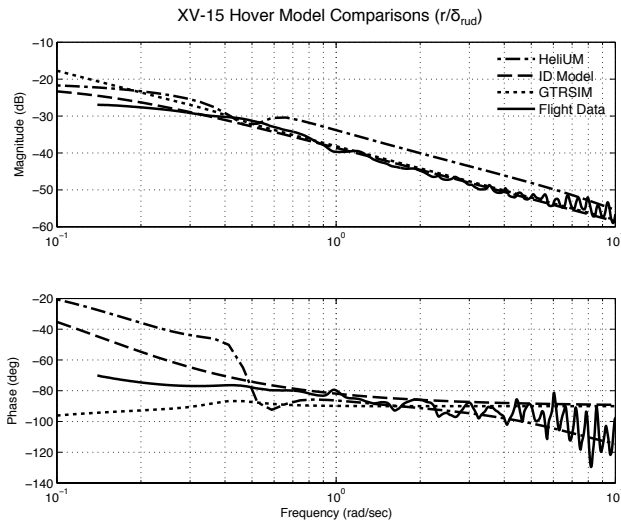


Fig. 7. XV-15 hover yaw rate response to pedal inputs.

Figure 8 shows the pitch rate response to longitudinal inputs. Here the curve marked “TF Model” comes from low order transfer functions found in Ref. 15. Flight data were not available for the pitch or heave responses, but the transfer function models were fit to flight data. The pitch

response is measured in rad/sec and the input is degrees of elevator deflection, which are geared with symmetric longitudinal cyclic swashplate commands. Much like the roll response, this curve is dominated by the low frequency phugoid pole. There is a difference in the low frequency slope of the curves; the TF Model predicts a 20 dB/dec slope, while the HeliUM model predicts a 40 dB/dec slope. This difference is again attributed to the modeling of the hub. The pitch response of the rotorcraft is a product of longitudinal flapping of each rotor and variations in hub type should produce different results. This is not seen in the roll response, Fig. 6 or heave response, Fig. 9, because these responses come from collective and rotor coning.

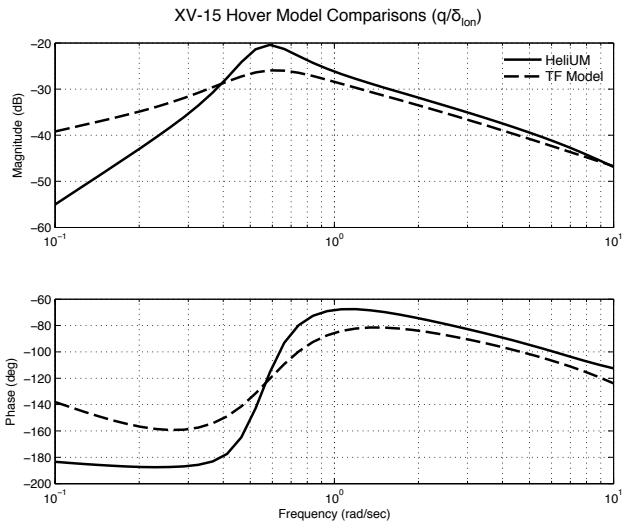


Fig. 8. XV-15 hover pitch rate response to longitudinal stick inputs.

Figure 9 shows the heave response to collective stick inputs. The HeliUM curves match well with the low order transfer function model. The slight difference in magnitude plots represents an error of less than 5%. The portions of the magnitude and phase curves between 1 and 10 rad/sec show a consistent heave response to commanded inputs at these frequencies. The transfer function model has a flat magnitude response because the effects of dynamic inflow are not included, although they are present in the HeliUM model.

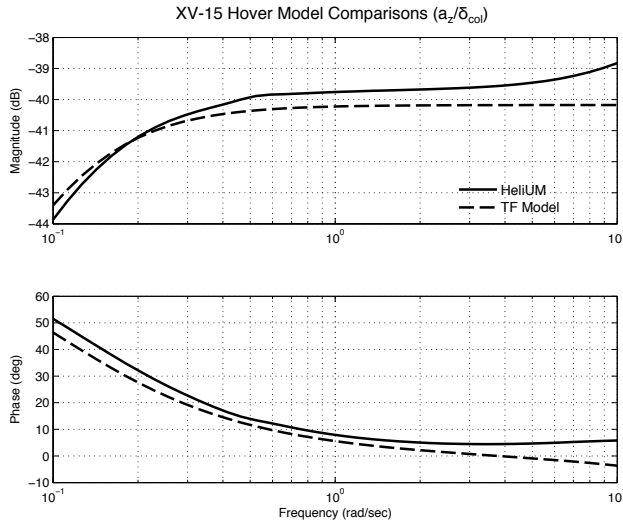


Fig. 9. XV-15 hover heave response to collective stick inputs.

Cruise: In cruise mode, the XV-15 behaves much like a fixed wing aircraft. Through transition to cruise, rotor symmetric and antisymmetric lateral cyclic controls are dialed back based on nacelle angle. At the cruise nacelle angle, the pilot lacks lateral cyclic control, and controls the roll of the aircraft through the ailerons. The cruise speed for the following plots is 180 knots.

Figure 10 shows the roll rate response to lateral stick commands. The units are the same as the hover configuration. The roll response is dominated by the Dutch roll mode at around 1.5 rad/sec, with a corresponding magnitude drop and phase decrease. The HeliUM model shows a slightly more damped Dutch roll oscillation, but the overall response matches well.

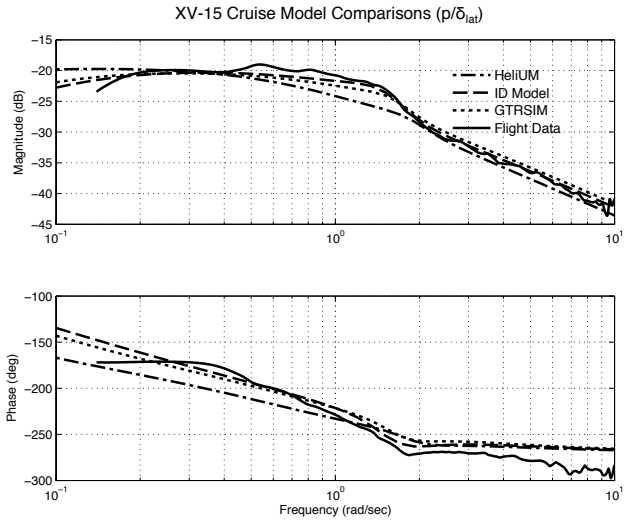


Fig. 10. XV-15 cruise roll rate response to lateral stick inputs.

The yaw response, Fig. 11, shows the yaw rate response in rad/sec to measured rudder inputs in degrees. The lightly damped zero at 0.45 rad/sec is followed by the Dutch roll peak, again at around 1.5 rad/sec. The damping of the zero for the HeliUM model is predicted slightly unstable, but overall the curve fits well with the other models and flight data.

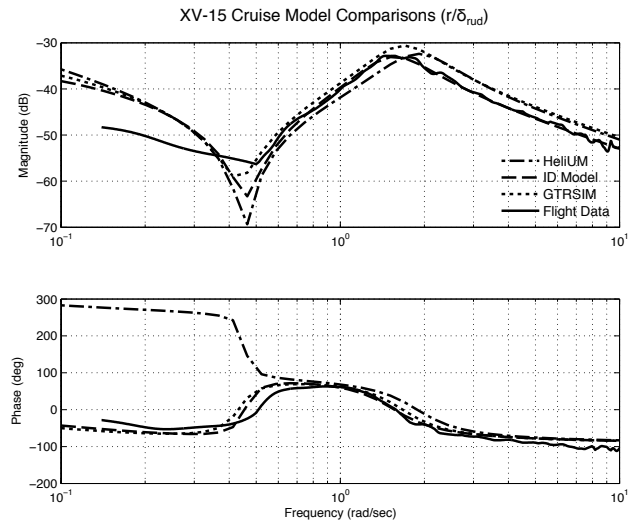


Fig. 11. XV-15 cruise yaw rate response to pedal inputs.

The pitch response in Fig. 12 shows the pitch response in rad/sec to measured elevator inputs in degrees. The transfer function model is a low order fit of the physical response and includes the lightly damped short period mode. The short period mode occurs at a slightly lower frequency in the transfer function model than it does in the HeliUM case. The gain and phase offset at low frequency can be attributed to phugoid dynamics which

are not included in the low order transfer function model.

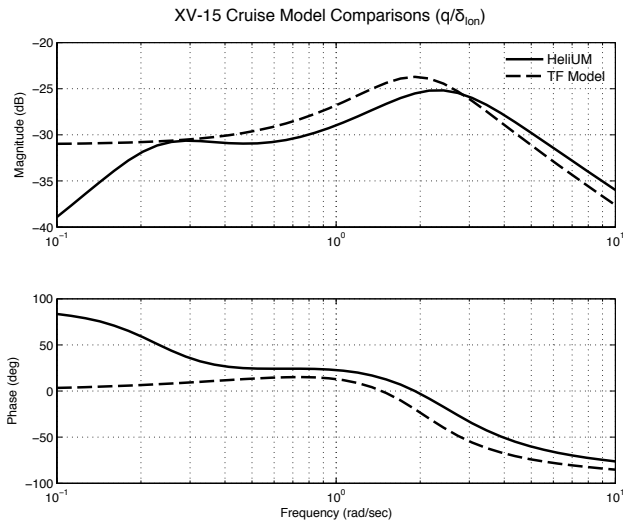


Fig. 12. XV-15 cruise pitch rate response to longitudinal stick inputs.

Overall, there is good agreement between the XV-15 HeliUM model, prior models, and flight data, validating the modeling approach taken.

LCTR Dynamics

The LCTR dynamics are next validated against CAMRAD. These models are then reduced to include only lateral/directional and wing bending states. The reduced order flexible wing models are then decoupled into rigid body portions and flexible wing portions. These decoupled models show the validity of deriving rigid body only models and adding structural flexibility to those models in parallel. Model following control laws are then developed for the full order and flexible wing models. It is shown that the flexible wing model has reduced stability and degraded handling qualities as compared to the rigid body aircraft. Notch filters are added to suppress the flexible wing contribution in the outputs and handling qualities are restored.

Full Order Validation

Full order LCTR models derived from HeliUM are compared to full order rigid body CAMRAD models. The models contained rotor, inflow, and rigid body states. The majority of the inputs for HeliUM come directly from the CAMRAD model. The HeliUM model contains two rotor modes; flap and lag.

Wing flexibility was also included in the validation (Figs.15-18) as a separate curve since the CAMRAD linear model did not include wing flexibility. The wing structural frequencies were derived to match those of Ref. 4, and

structural damping was set to 4 %. Wing beamwise bending stiffness was modified until the antisymmetric beamwise bending mode occurred at approximately 16.5 rad/sec. Likewise, chordwise stiffness was modified until a frequency of 14.5 rad/sec was reached for the antisymmetric chordwise bending mode. Since the pylon is displaced vertically from the elastic axis, the chordwise mode contains heavily coupled chordwise and torsion motion. Mode shapes for the LCTR are shown in Figs. 13 and 14. Each mode has a symmetric and antisymmetric component. The wing modes show up as second order poles and are accompanied by decreases in phase. The validation results look at both the longitudinal as well as lateral/direction axes.

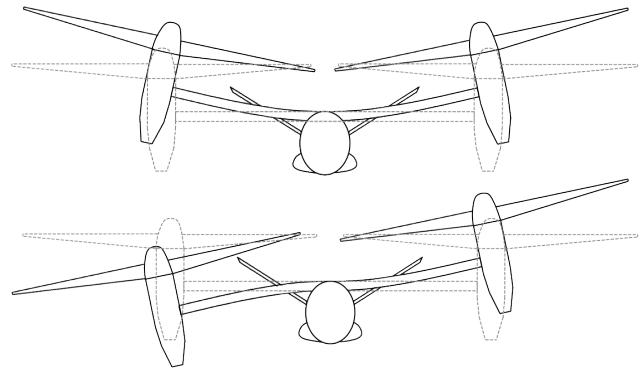
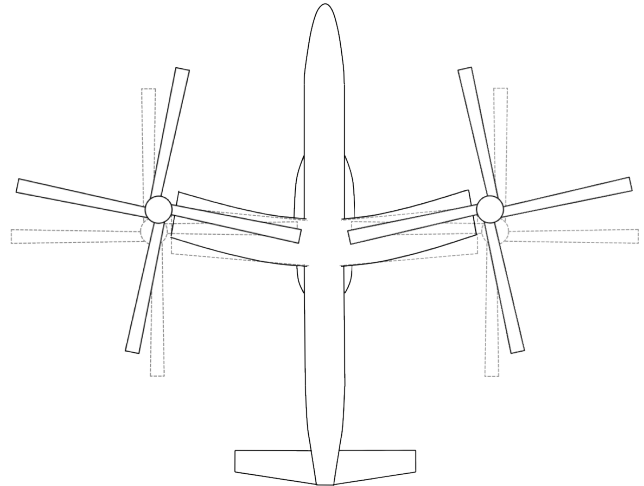


Fig. 13. LCTR symmetric and antisymmetric beamwise bending mode shapes



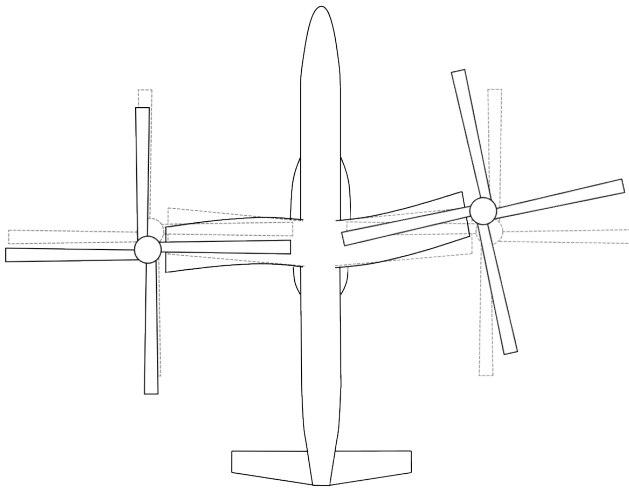


Fig. 14. LCTR symmetric and antisymmetric chordwise bending mode shapes

The LCTR modal frequencies could also be estimated if the XV-15 structural modes are known. Froude scaling suggests that the structural frequencies of the aircraft will reduce with the square root of the vehicle size ratio (Ref. 17). The LCTR has a rotor radius of 32.5 feet, and the XV-15 rotor had a 12.5 foot radius, giving a ratio of 0.38. The first symmetric structural mode, derived from XV-15 flight test results, occurs at 20.7 rad/sec, giving an estimate of 12.8 rad/sec for the LCTR. The first symmetric coupled rigid-body/wing mode from the model occurs at 9.9 rad/sec. Using Froude scaling alone would suggest that including the structural frequencies of the LCTR would be important for flight controls applications. The scaling isn't exact, but provides a good rule of thumb estimation for mode scaling.

Figures 15 through 18 compare the CAMRAD and HeliUM models. Overall there is good agreement in all axes for the rigid wing HeliUM curves and the CAMRAD curves up to about 30 rad/sec. The rigid wing curves don't include any structural flexibility, while the flex wing curves have a rigid fuselage with flexible wings. The output magnitudes are expressed in deg/sec or ft/sec. Inputs are inches of stick deflection. Rotor modes also match well. The first flap mode from HeliUM is at 1.44/rev and for CAMRAD is at 1.43/rev. The models all match well at low frequency and diverge at the frequency of the wing mode, as expected, because flexible wing modes are highly coupled to rigid body states.

The roll response, Fig. 15, is dominated by the lateral phugoid at low frequency. When comparing the CAMRAD and rigid wing HeliUM curves, there are offsets only at the higher frequencies corresponding to rotor dynamics. The large peak in the magnitude in the flexible wing response around 16 rad/sec is the wing antisymmetric beam mode. It will be shown that this mode corresponds to the anti-symmetric beamwise bending mode mentioned earlier. At frequencies above the wing mode, the flexible wing HeliUM curve has characteristics similar to the other curves.

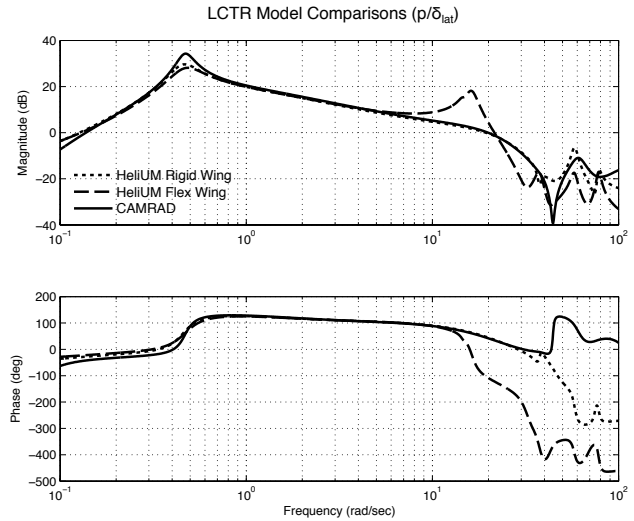


Fig. 15. LCTR hover roll rate response to lateral stick inputs.

The yaw response, Fig. 16, is similar to that of the XV-15, Fig. 7, and shows a fairly constant -20 dB/dec slope in the magnitude plot. The low frequency first order yaw mode causes the slope change in the magnitude plot and associated 90 deg phase decrease. As with the roll case, and with the rest of the plots, rotor dynamics start to have a dominant effect at around 30 rad/sec. The wing structural peak, at around 14 rad/sec, is associated with the antisymmetric chordwise wing bending mode as indicated earlier. This is a coupled mode because of the nacelle's inertia. The nacelle acts as a large mass above the elastic axis of the wing. It does not effect beamwise bending but creates large torsion moments during chordwise bending.

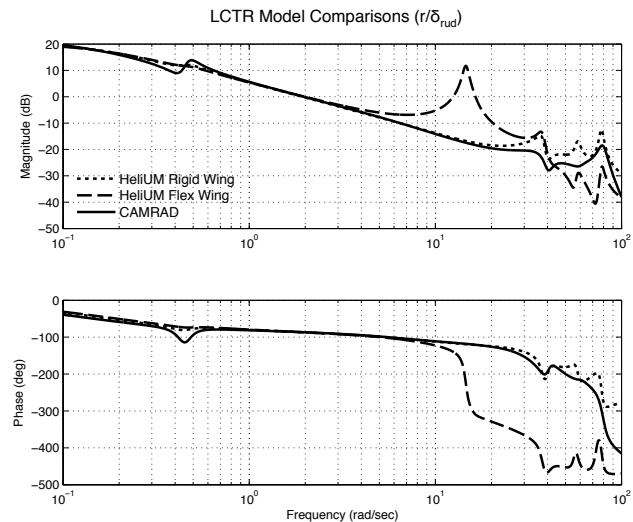


Fig. 16. LCTR hover yaw rate response to pedal inputs.

The HeliUM model was not able to capture the low frequency XV-15 pitch response well (Fig. 8), and this was attributed to the rotor hub modeling. The LCTR has a hin-

geless rotor system which forces the blades to behave as cantilevered beams. HeliUM models this type of blade boundary condition and the response now matches well with CAMRAD results (Fig. 17). The wing flexibility contribution here comes from coupled symmetric chordwise beam bending and torsional displacements. This mode is the symmetric counterpart to the wing mode in the yaw response.

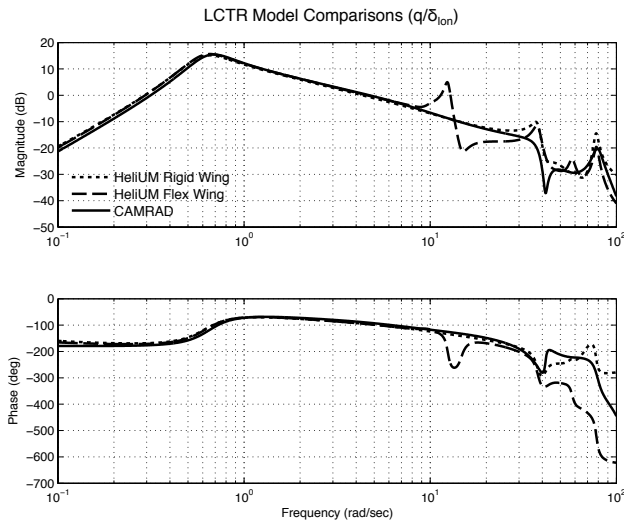


Fig. 17. LCTR hover pitch rate response to longitudinal stick inputs.

The vertical velocity response of the rigid body HeliUM case matches well with the CAMRAD plot, and is shown in Fig. 18. The wing bending mode excited here is a symmetric beamwise bending mode, the counterpart to the antisymmetric mode in the roll response.

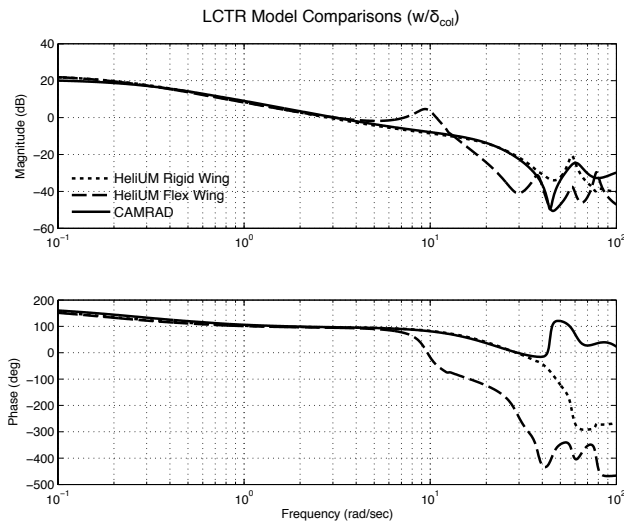


Fig. 18. LCTR hover vertical velocity to collective inputs.

Reduced Order Models

Reduced order models offer the ability to evaluate the overall aircraft response in terms of conventional stability and control derivatives. In the reduced order models shown, only lateral/directional rigid body states are retained along with the relevant wing structural modes if wing flexibility is included. All the models used come from HeliUM. Table 2 summarizes the states kept and the nomenclature used for the reduced models. Longitudinal rigid body, rotor, inflow, and non-relevant wing states are reduced out using a quasi-static reduction. The “Rigid Wing” model contains 47 states, while the “Lat/Dir Rigid Wing” contains only 5 total states (including yaw angle, ψ). The “Flex Wing” model contains 55 states, all the states of the Rigid Wing model and an additional 8 wing structural states. The “Lat/Dir Flex Wing” contains 9 states, including 5 rigid body states and 4 states associated with two antisymmetric wing bending modes. The lateral axis excites, almost exclusively, the antisymmetric beamwise bending mode, while the directional axis excites the antisymmetric chordwise/torsion mode. Figures 19 and 20 show reduced order models. The full order curves are retained for comparison.

The Lat/Dir Rigid Wing roll response matches well with the full order Rigid Wing model, which also includes rotor dynamics, at low frequency, meaning the system is well decoupled from longitudinal dynamics, as expected for a tiltrotor in hover. Divergence occurs in the magnitude plot around 8 rad/sec, well within the frequency range of interest for control systems design. Rotor modes are important even at this low frequency and using a reduced order model might lead to an inaccurate stability and handling qualities analysis. The Lat/Dir Rigid Wing phase response diverges from the full order response at higher frequency than the magnitude plot. The wing mode excited in the Lat/Dir Flex Wing case is the antisymmetric beamwise bending mode. The other wing modes have a negligible impact on the roll response. The included wing bending mode captures well the dynamics around the frequency of the wing mode. There are slight gain and phase differences around the frequency range of the mode. These differences could be attributed to effects from the other flexible wing modes, but clearly, the dominant response is captured.

	Longitudinal Rigid Body	Lateral/Directional Rigid Body	Inflow	Rotor	Symmetric Structural	Antisymmetric Structural
Rigid Wing	✓	✓	✓	✓		
Flex Wing	✓	✓	✓	✓	✓	✓
Lat/Dir Rigid Wing		✓				
Lat/Dir Flex Wing		✓				✓

Table 2. Reduced order model nomenclature

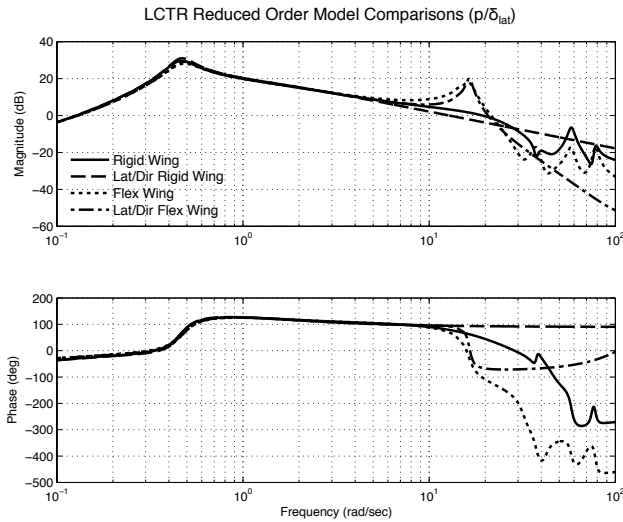


Fig. 19. LCTR reduced order hover roll response comparisons with full order models

The Lat/Dir Rigid wing yaw response matches well at low frequency in the magnitude plot. Pedal inputs produce differential longitudinal cyclic commands to the rotor. The tip path plane must realign in order to produce differential force and thus yaw moments. This realignment produces a time delay, and thus the phase diverges at lower frequencies than the roll response since the rotor responds to lateral stick commands through collective inputs which achieve a response from the system much faster than cyclic inputs. The phase difference in the rigid wing reduced model could be accounted for with a time delay. The time delay is approximately 0.04 seconds. For the LCTR rotor with a flap frequency of 1.44/rev, a 1/rev input leads to a delay of approximately 0.04 seconds before realignment of the tip path plane, which matches the time delay from the phase offset. Rotor dynamics therefore play a large role in the yaw response. Time delays could be used to improve the phase difference. Magnitude plots, however, are not affected by time delays, so the variations between the reduced order and full order magnitude plots would still produce significant error in flight control applications. The Lat/Dir Flex Wing case contains the antisymmetric chordwise/torsion bending mode. This is the only mode significantly excited by this response.

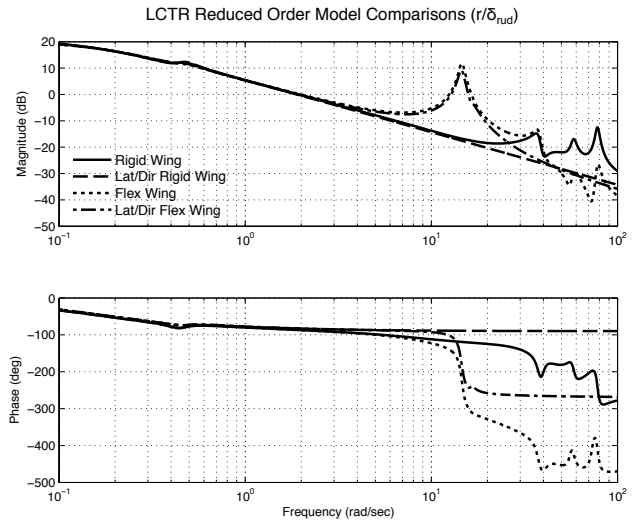


Fig. 20. LCTR reduced order hover yaw response comparisons with full order models

LCTR Structural Coupling Analysis

In general, the flexible wing modes are highly coupled with rigid body motion of the aircraft. As seen in Figs 15 through 18, each rigid body response has a flexible wing mode associated with it. Symmetric wing bending modes couple with longitudinal motion of the aircraft, while antisymmetric modes tend to couple with lateral/directional motion. The reduced order model from Fig. 19 still captures the structural response with only the antisymmetric beamwise bending mode included. The reduced order model from Fig. 20 retains the response if only the antisymmetric chordwise bending mode is included. It has been shown that the reduced order models may not be accurate for flight control design. Reduced order models are useful for understanding effects of structural flexibility on broader aircraft metrics such as stability and control derivatives. This section describes the effect of decoupling the structural modes from the rigid body. Regaining the fully coupled response is then attempted by augmenting the output matrix to include structural flexibility.

The general states space structure is.

$$\begin{aligned} \{\dot{x}\} &= [A] \{x\} + [B] \{u\} \\ \{y\} &= [C] \{x\} + [D] \{u\} \end{aligned} \quad (19)$$

The state vector can be reorganized into parts containing rigid body terms and parts containing structural flexibility terms.

$$\{x\} = \begin{Bmatrix} x_{rb} \\ x_{str} \end{Bmatrix} \quad (20)$$

A reduced order model with wing flexibility can be decomposed into blocks that follow the nomenclature in References 17, 19:

$$A = \left[\begin{array}{c|c} \text{Rigid - Body} & \text{Aeroelastic} \\ \text{Stability} & \text{Coupling} \\ \text{Derivatives} & \text{Terms} \\ \hline \text{Rigid - Body} & \text{Structural} \\ \text{Coupling} & \text{Flexibility} \\ \text{Terms} & \text{Modes} \end{array} \right] \quad (21)$$

$$B = \left[\begin{array}{c} \text{Rigid - Body} \\ \text{Control} \\ \text{Derivatives} \\ \hline \text{Structural} \\ \text{Mode Control} \\ \text{Derivatives} \end{array} \right] \quad (22)$$

If starting from a rigid body model, to implement a fully decoupled system, structural dynamics could be added to the rigid body equations in block diagonal form. The wing contribution to the roll response is added to the model through the output. If the rigid body roll response is implemented as a SISO system, the transfer function could have the following form (Ref. 17).

$$\frac{P}{\delta_{lat}} = G_{rb}(s) + G_{str}(s) \quad (23)$$

$$\begin{aligned} \frac{p}{\delta_{lat}} &= \frac{L\delta_{lat}}{s - L_p} + \frac{\eta_1 \delta_{lat} s}{s^2 + 2\zeta_1 \omega_1 s + \omega_1^2} + \dots \\ &+ \frac{\eta_n \delta_{lat} s}{s^2 + 2\zeta_n \omega_n s + \omega_n^2} \end{aligned} \quad (24)$$

In block form, this is as the same as adding structural dynamics in parallel as shown in Fig. 21 and suggested in Ref. 18.

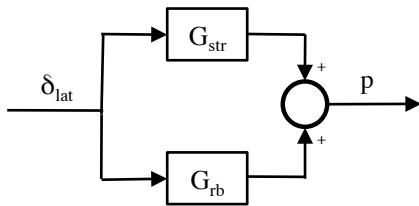


Fig. 21. Parallel implementation of structural and rigid body dynamics

A first attempt to decouple the system from one that has the form of Eqn. (21) to one like Eqns. (23) and (24), can be done by zeroing out the off diagonal components. However, Aeroelastic Coupling Terms couple structural flexibility back into the rigid body equations of motion. If the Aeroelastic Coupling Terms are forced to be zero, there will be no structural flexibility effect to the rigid body states, so the contribution from flexibility must be added to the output matrix. Also, the Rigid Body Coupling Terms couple rigid body motion back into the structural mode equations and give the terms in Eqn. (24) an additional s^0 term in the partial fraction expansion (Ref. 17).

If there is enough separation between the frequency of the highest rigid body mode and the structural mode of interest,

$$\frac{\omega_{str}}{\omega_{rb}} \geq 5, \quad (25)$$

the aeroelastic coupling contributions to rigid-body motion can be absorbed into the Rigid-Body Stability Derivatives through a quasi-static reduction of the wing structural modes (Ref. 17). The reduction of the wing structural states from the Lat/Dir Flex Wing model into the rigid-body states produces a *static-elastic* model with only rigid-body states. The differences between the rigid-body stability derivatives from the Lat/Dir Rigid Wing and the static-elastic derivatives are known as *flex factors*. Table 3 gives the nomenclature of the models used in this analysis.

Roll and yaw responses to stick inputs for Lat/Dir Rigid Wing, Static-Elastic and Lat/Dir Flex Wing models are shown in Figs. 22 and 23. The Static-Elastic model is the Lat/Dir Flex Wing model with structural modes reduced out and thus these models match very well with each other in both axes at low frequency. These two models are expected to match well because the inequality of Eqn. (25) holds. Both models predict the flex wing response well up to $\omega_{str}/3$. Table 4 contains the eigenvalues for the lateral/directional model and shows that the frequency separation is greater than 10. The table contains both the antisymmetric beam-wise bending mode which is excited in the roll response and antisymmetric chordwise/torsional bending mode which is excited in the yaw response.

	Rigid-Body Stability Derivatives	Flex Factors	Aeroelastic Coupling Terms	Rigid-Body Coupling Terms	Structural Flexibility Mode
Lat/Dir Rigid Wing	✓				
Lat/Dir Flex Wing	✓		✓	✓	✓
Static-Elastic	✓	✓			
Static-Elastic with RBC	✓	✓		✓	✓
Decoupled Flexibility	✓	✓			✓

Table 3. Decoupling analysis model nomenclature

Eigenvalue	ζ	ω_n (rad/sec)	Mode
-1.65e-01	1.00e+00	1.65e-01	Spiral
8.36e-02 + 4.68e-01i	-1.76e-01	4.76e-01	Lateral
8.36e-02 - 4.68e-01i	-1.76e-01	4.76e-01	Phugoid
-1.19e+00	1.00e+00	1.19e+00	Roll
-5.67e-01 + 1.45e+01i	3.91e-02	1.45e+01	Antisymmetric Chordwise/ Torsion Bending
-5.67e-01 - 1.45e+01i	3.91e-02	1.45e+01	
-6.22e-01 + 1.65e+01i	3.78e-02	1.65e+01	Antisymmetric Beamwise Bending
-6.22e-01 - 1.65e+01i	3.78e-02	1.65e+01	

Table 4. Eigenvalues for the Lat/Dir Flex Wing LCTR model

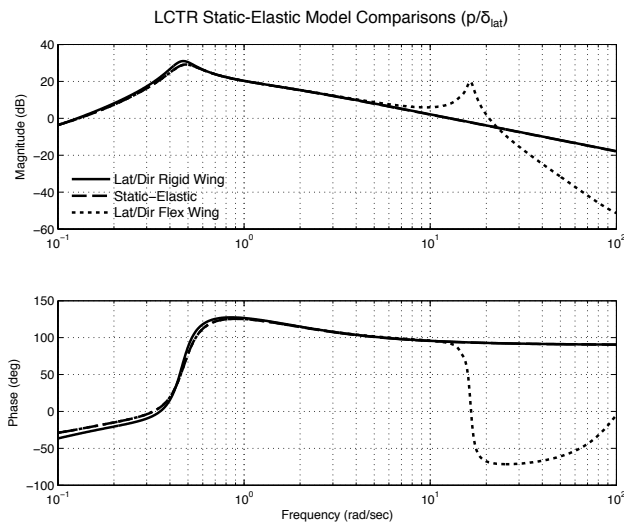


Fig. 22. Model reduction comparisons for a roll response to lateral stick inputs

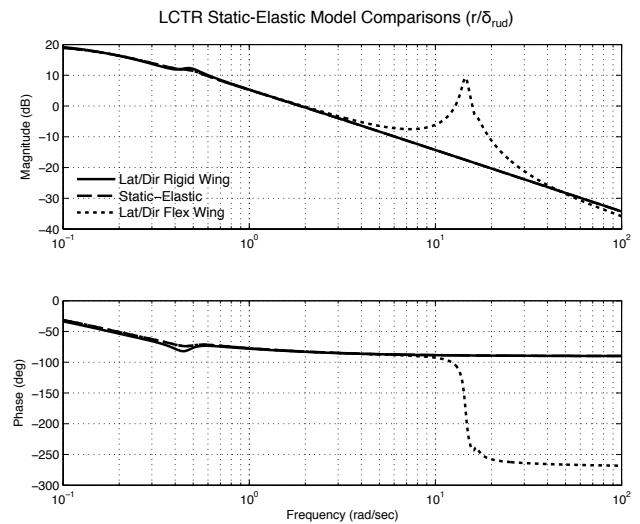


Fig. 23. Model reduction comparisons for a yaw response to pedal inputs

Flex factors quantify the change in the Static-Elastic model as compared to the original Lat/Dir Rigid model and show the influence of structural flexibility on the rigid-body stability derivatives. Flex factors for key stability and control derivatives are given in Table 5.

	Rigid-Body	Static-Elastic	Flex Factor
Y_v	-0.0728	-0.0435	0.5968
L_p	-0.9661	-0.9572	0.9908
N_v	0.0009	0.0007	0.7970
N_r	-0.1819	-0.1874	1.0304
$L_{\delta_{lat}}$	-0.2250	-0.2219	0.9864
$N_{\delta_{lat}}$	0.0249	0.0259	1.0389
$L_{\delta_{ped}}$	-0.0427	-0.0459	1.0748
$N_{\delta_{ped}}$	0.0337	0.0336	0.9982

Table 5. Comparison of Lat/Dir Rigid Wing and Static-Elastic stability and control derivatives

The flex factors for stability derivatives L_p and N_r , as well as control derivatives $L_{\delta_{lat}}$ and $N_{\delta_{rud}}$, are nearly one. This could have been inferred from the Figs. 22 and 23 because the Static-Elastic response matches so well with the Lat/Dir Rigid Wing response. The difference in the Y_v stability derivative could account for the small difference in the lateral phugoid peak between the Lat/Dir Rigid Wing and Static-Elastic roll responses as Y_v is a component of the hovering cubic. The hovering cubic does not show up in a first order yaw response, so this stability derivative does not have a large impact on the yaw response.

Including flex factors in the Rigid-Body Stability Derivatives allows for the zeroing out of the Aeroelastic Coupling Terms. The Rigid-Body Coupling Terms (RBC) are still retained, so the equations are still not fully decoupled. The damping and natural frequency of the structural mode is set to the damping and natural frequency of the mode in the fully coupled system. This is done because any system rewritten in block diagonal form must retain the eigenvalues of the original system. With the exclusion of the Aeroelastic Coupling Terms, in order to add the contribution to wing flexibility in the overall response, the output matrix must be augmented to include wing structural modes. The contribution to the roll response of the output is taken from the wing rate state. The roll response output will now be:

$$p = p' + \Phi_{p1} \dot{q}_{str1} \quad (26)$$

Here, p' is the roll response from the static-elastic model, Φ_{p1} is the contribution to roll from the first structural mode and is called an influence coefficient, and \dot{q}_{str1} is the rate component from the first structural mode. In the current formulation, the influence coefficient can be calculated as the ratio of aeroelastic coupling to the natural mode of the structural frequency (Ref. 17).

$$\Phi_{p1} = \frac{L_{q_{str1}}}{\omega_{str1}^2} \quad (27)$$

Figures 24 and 25 show the roll and yaw response of the aircraft to lateral stick and pedal inputs, respectively. The Lat/Dir Flex Wing curves retain the rigid-body lateral/directional and structural states intact. The ‘‘Static-

Elastic with RBC’’ curves reduce out the Aeroelastic Coupling Terms and use the static-elastic model, as well as the output matrix, as described above, to retain the effects of wing bending.

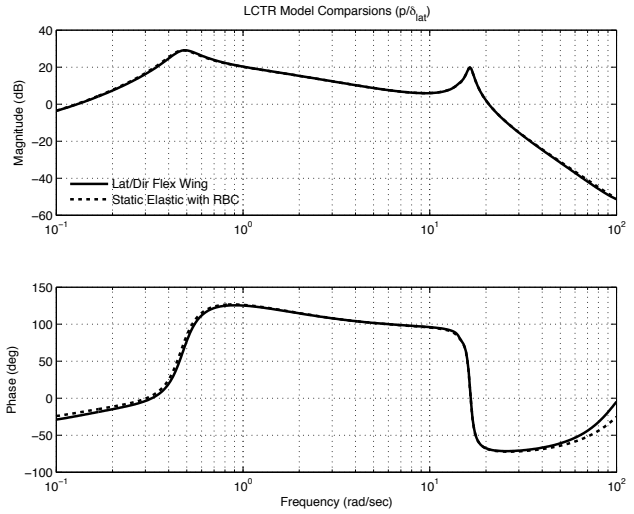


Fig. 24. Model comparisons for roll response to lateral stick inputs.

Both the roll and yaw responses show very good agreement with the Lat/Dir Flex Wing models up to the wing structural frequencies. Above the wing structural frequencies, there are some small discrepancies, particularly in the phase plots.

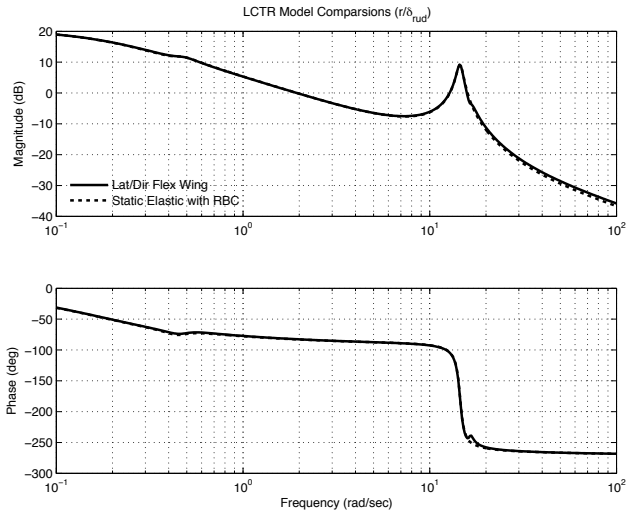


Fig. 25. Model comparisons for yaw response to pedal inputs.

The final step in decoupling the system is to remove the Rigid-Body Coupling Terms from the Static-Elastic with RBC model described above. These terms couple the rigid-body motion to the wing (Eqn. (21)). The fully decoupled roll and yaw responses, of the form of Eqn. (24), are plotted against the fully coupled response in Figures 26 and 27. The Rigid-Body Coupling Terms will have a negligible effect on

the dynamics if the following inequality holds (Ref. 17):

$$\left| \frac{\omega_1}{z_1} \right| \geq 5 \quad (28)$$

Here z_1 is the first partial fraction zero of a system that includes Rigid-Body Coupling Terms, but otherwise is of the same form as shown in Eq. 24.

$$\begin{aligned} \frac{p}{\delta_{lat}} = & \frac{L_{\delta_{lat}}}{s - L_p} + \frac{\eta_{10}\delta_{lat} + \eta_{11}\delta_{lat}s}{s^2 + 2\zeta_1\omega_1s + \omega_1^2} + \dots \\ & + \frac{\eta_{n0}\delta_{lat} + \eta_{n1}\delta_{lat}s}{s^2 + 2\zeta_n\omega_ns + \omega_n^2} \end{aligned} \quad (29)$$

with

$$z_n = \frac{\eta_{n0}\delta_{lat}}{\eta_{n1}\delta_{lat}} \quad (30)$$

This first partial-fraction zero of Eq. 29 can be approximated as (Ref. 17):

$$z_1 \cong \frac{L_{\delta_{lat}}\eta_{1p}}{\eta_{11}\delta_{lat}} \quad (31)$$

Here, η_{1p} is the rigid-body coupling term that couples the roll response to the wing mode and $\eta_{11}\delta_{lat}$ is the control derivative for the wing mode. For the yaw response, the approximate zero using Eqn. (31) is $z_{1approx} = 0.0246$. The exact zero is $z_{1exact} = 0.025$. With the wing structural mode occurring at $\omega_{\eta_1} = 14.5$ rad/sec, the Rigid-Body Coupling Terms can be safely ignored in the yaw response. The roll response has a $z_{1approx} = 1.65$ and $z_{1exact} = 1.81$. The wing structural mode occurs at $\omega_{\eta_1} = 16.5$ rad/sec, therefore the Rigid-Body Coupling Terms can also be ignored in the roll response.

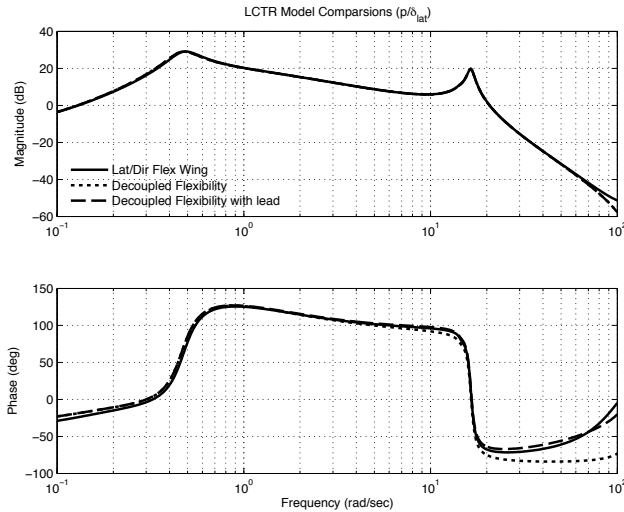


Fig. 26. Coupled flexible wing and decoupled model comparisons for roll response to lateral stick inputs.

The decoupled roll response in Fig. 26 shows good agreement in magnitude. The phase curve shows good

agreement up to the structural frequency, but diverges afterwards. The most significant of the rigid body coupling stability derivatives is the roll effect on wing state, η_{1p} . Replacing this term would restore the roll response seen in Fig. 24. A small phase lead of 10 msec is added as the final curve to improve the phase response at higher frequencies. The yaw response matches well over the entire frequency range in magnitude and phase, and a phase lead is not necessary to improve the correlation to the Lat/Dir Flex Wing model. For this response, the effects of rigid body coupling are insignificant and the η_{1r} stability derivative is small.

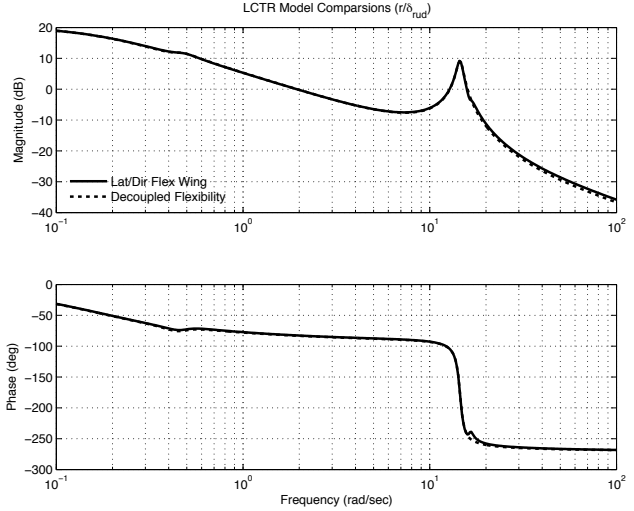


Fig. 27. Coupled flexible wing and decoupled model comparisons for yaw response to pedal inputs.

The results above show that even with a fully decoupled flexible wing response, i.e. Fig 21, accurate dynamics of the aircraft can be reproduced. From a system identification and flight dynamics simulation standpoint, this means that a large model with many unknowns is not necessary. Rigid body stability and control derivatives, a few number of structural coefficients, and time delays are capable of reproducing the response.

LCTR Control Design

The final section of this paper discusses the control design for the flexible wing LCTR using *The Control Designer's Unified Interface* (CONDUIT[®]) software tool (Ref. 20). The same control architecture is used as described in Refs. 7–9 and is shown in Fig. 29. The model following controller is designed for all axes and thus also contains longitudinal dynamics. Control laws were developed for the full order rigid and flexible wing HeliUM models, labeled Rigid Wing and Flex Wing in previous sections of this paper. A third set of control laws used the same Flex Wing model, but also included notch filters at the outputs and feedforward loop to remove the wing flexibility effects from the dynamics of the aircraft. Only the model and use of notch filters was substituted in each case, while the rest of the

controller architecture remained unchanged. The command model gives an attitude command attitude hold (ACAH) response type in the roll and pitch axes and rate command in the yaw axis. The inverse plant contains first order fits of the short-term aircraft on-axis response between 1 and 10 rad/sec. The time delay block is introduced to avoid overdriving actuators and other higher order dynamics that are not modeled by the first order inverse block. The time delays are equal to the system response delays to command inputs. The actuator block introduces limits on actuators positions and rates and allows for evaluation of PIO tendencies.

Notch filters were fit on the outputs of the model to remove components of the vehicle response caused by excitation of the wing structural modes. They were added to the roll, pitch, and yaw feedbacks and were tuned to the wing structural mode excited by each response. Notch filters were also added at the feedforward path. This prevented the command model from exciting a wing structural mode. These notch filters were added to the commanded stick inputs, and each stick displacement's notch filter was tuned to the wing mode that was excited by that command. The notch filters used are shown in Fig. 28. The damping of the numerator and denominator of each filter were hand tuned.

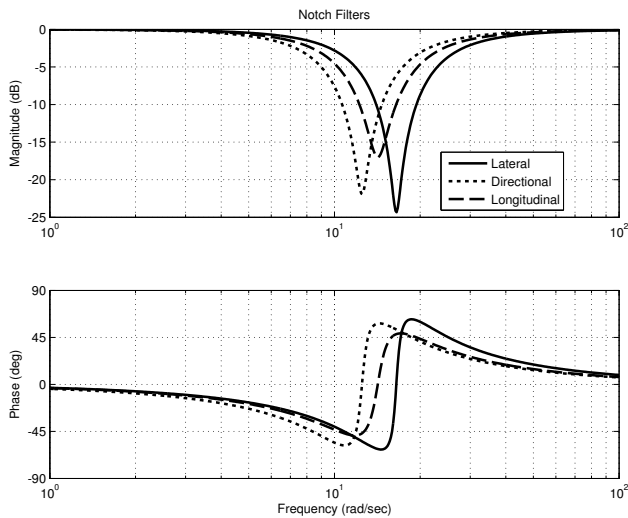


Fig. 28. Notch filters for the lateral, directional, and longitudinal axes

The optimization focused on the lateral/directional axis, though a longitudinal stability margin specification was used to help ensure stable longitudinal modes at low frequency. Table 6 presents the specifications used in the CONDUIT[®] optimization.

Vertical acceleration at the CG was also fed back to help stabilize a coupled heave/wing symmetric beamwise bending mode. The feedback attempts to directly control this structural mode. It was found that a positive (i.e. destabilizing) feedback was beneficial at reducing the higher frequency vertical accelerations caused by this mode. The frequencies and damping ratios of the wing

structural modes were set to predetermined values, but coupled rigid-body/wing modes tend to have different damping ratios and frequencies. Positive displacements in vertical body states would normally elicit an increase in collective control to offset the downward motion of the aircraft. With flexible wings an increase in collective exacerbates the wing bending, exciting the wing structural mode, so a decrease in collective with $+\dot{w}$ is beneficial. At low frequency, vertical velocity and integral position feedback give the dominant response.

Figures 30 and 31 show the broken loop responses of the controller. The loops were broken at the actuators. The broken loop responses are used to calculate the stability margins of the aircraft, given in Table 7, along with the crossover frequencies. The control systems are designed to have a broken loop crossover frequency of $\omega_c = 2.7$ rad/sec in the lateral axis and $\omega_c = 2.0$ rad/sec in the yaw axis. The desired crossover frequencies were not reached in the flexible wing directional response with no notch filters and is due to a wing structural mode. The flexible wing response does not produce Level 1 stability margins in the roll or yaw axis. Both responses show the effect of the notch filters at reducing magnitude near the structural frequency of the wing. The notch filters, even with the added phase delay, bring the stability margins back to Level 1 and the crossover frequencies back to desired values.

Figures 32 and 33 show the Nichols plots for the broken loop response. These figures make it apparent that the flexible wing model without the notch filters is unacceptable.

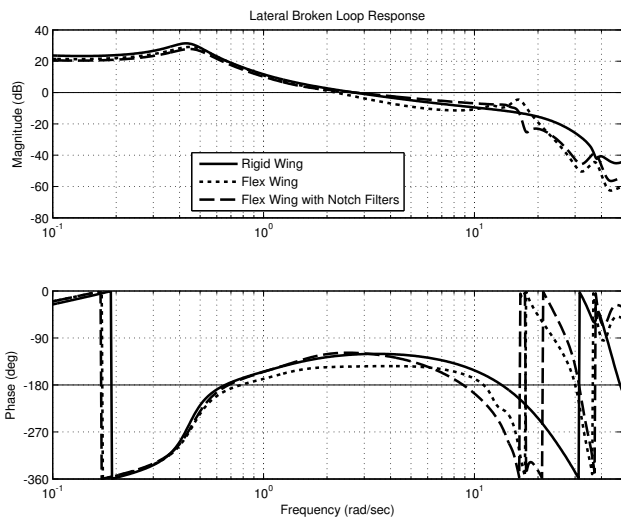


Fig. 30. Lateral broken loop response

Constraint	Spec Name	Description	Axis
Hard	EigLcG1	Eigenevalues in L.H.P	-
	StbMgG1	Gain Phase Margin (6 dB, 45 deg) ¹	Pitch, Roll, Yaw
	StbMgG2	Structural Gain Phase Margin (8 dB, 60 deg)	Pitch, Roll, Yaw
	ModFoG2	Model Following ²	Roll, Yaw
	DstBwG1	Disturbance Rejection Bandwidth	ϕ, ψ
Soft	DstPkG1	Disturbance Rejection Peak	ϕ, ψ
	CrsMnG2	Minimum Crossover Frequency ³	Roll, Yaw
	EigDpG1	Eigenvalue Damping (Below Piloted BW) ⁴	-
	EigDpG1	Eigenvalue Damping (Above Piloted BW) ⁴	-
	OlOpG1	Open Loop Onset Point (Actuator Rate Limiting)	Roll, Yaw
	DmpTmG1	Time Domain Damping (Pilot Input)	Roll
	DmpTmG1	Time Domain Damping (Disturbance Input)	ϕ
Summed Obj.	CrsLnG1	Crossover Frequency	Roll, Yaw
	RmsAcG1	Actuator RMS	Roll, Yaw
Check Only	BnwAtH1	Bandwidth (Other MTEs, UVE > 1)	Roll
	BnwYaH2	Bandwidth (Other MTEs)	Yaw

¹ 6dB, 45 deg. margins were not achievable for the Flex Wing model without notch filters.

² Model following max frequency was reduced from 10 rad/sec to 4 rad/sec for both Flex Wing cases.

³ Crossover frequencies were reduced for the Flex Wing model without notch filters.

⁴ Damping requirements were reduced for the Flex Wing models.

Table 6. Control system optimization specifications

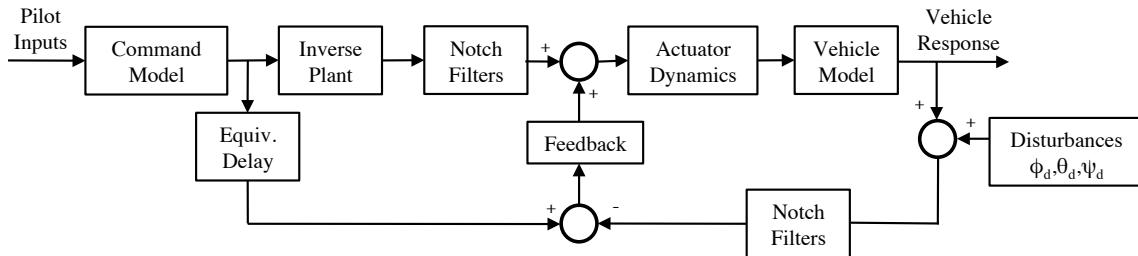


Fig. 29. Generic model following control system architecture

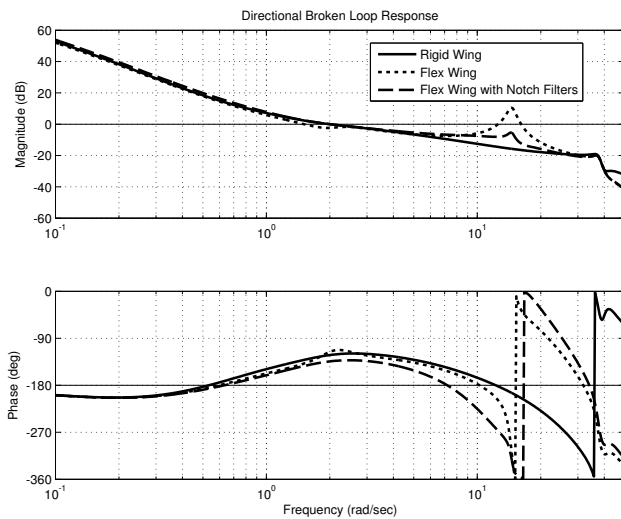


Fig. 31. Directional broken loop response

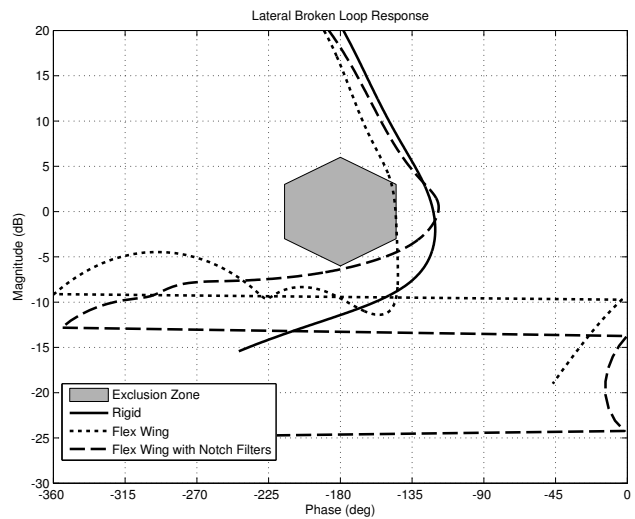


Fig. 32. Lateral broken loop Nichols plot

	Rigid Wing	Flex Wing	Flex Wing with Notch Filters
Lateral ω_c [rad/sec]	2.7	2.2	2.7
Directional ω_c [rad/sec]	2	1.5	2
Lateral PM [rad/sec]	58	35	61
Lateral GM [dB]	11	9.6	6.4
Directional PM [rad/sec]	58	28	46
Directional GM [dB]	14	5.5	6.7
Lateral ω_{BW} [rad/sec]	2.5	3.7	3.2
Lateral τ_{PD} [sec]	0.08	0.2	0.2
Directional ω_{BW} [rad/sec]	2.1	3.1	2
Directional τ_{PD} [sec]	0.072	0.2	0.22
ζ_{BW} [ND]	0.35	0.35	0.38
ζ_{Struct} [ND]	0.62	0.064	0.1
ϕ -DRB [rad/sec]	0.97	1.1	0.91
ϕ -DRP [dB]	3.5	6.3	2.9
ψ -DRB [rad/sec]	0.6	0.65	0.73
ψ -DRP [dB]	4.1	6	4.4

Table 7. Handling Qualities Comparison

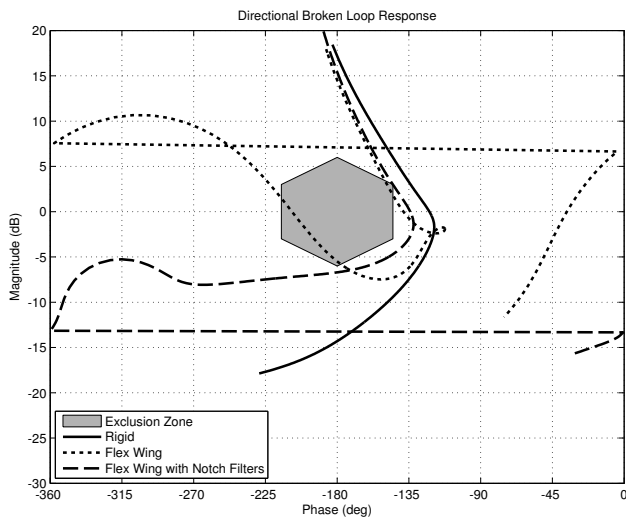


Fig. 33. Directional broken loop Nichols plot

Root locus plots for roll feedback are shown next in Figs. 34, 35, and 36. These plots show the effect of wing flexibility at reducing the allowable control system gains before instability occurs. The rigid wing response, Fig. 34, allows a high gain before a rotor mode becomes unstable, and there is a large separation between the design gain used in the Rigid Wing control laws and the instability.

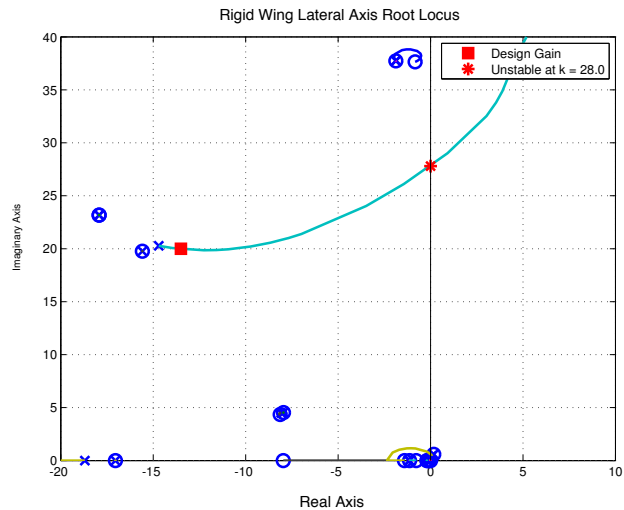


Fig. 34. Root locus plot for roll feedback on the rigid wing model

The Flex Wing root locus plot, Fig. 35, gives a much tighter allowance between the design gain and the gain when the first mode becomes unstable, which is the wing antisymmetric beamwise bending mode, as expected for a roll rate feedback. The pilot, if acting as a gain, could easily destabilize the wing bending mode.

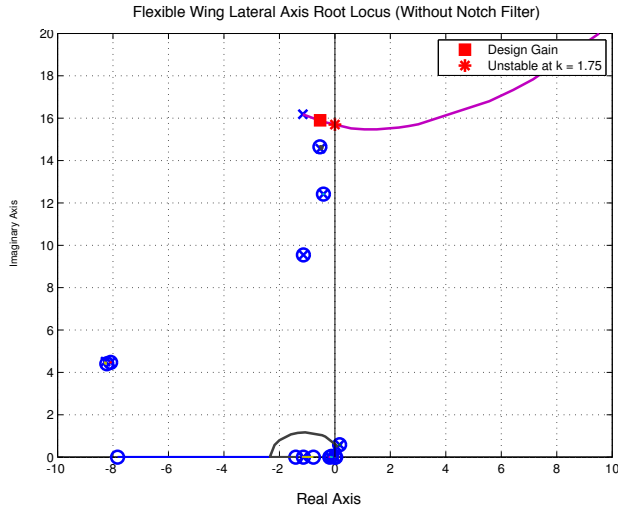


Fig. 35. Root locus plot for roll feedback on the flexible wing model

The root locus plot for the Flex Wing model with a notch filter is shown in Fig. 36. This figure shows the effect of the notch filter zero at attracting the wing mode and preventing it from becoming unstable. The notch filter does not add damping to the wing mode, but does allow for higher gains in the roll rate feedback before instability occurs. The first mode to go unstable here is the pole of the notch filter, but it does so at a much higher gain than if the notch filter was not used, giving a higher gain separation, or gain margin, than the flexible wing case without the notch filters.

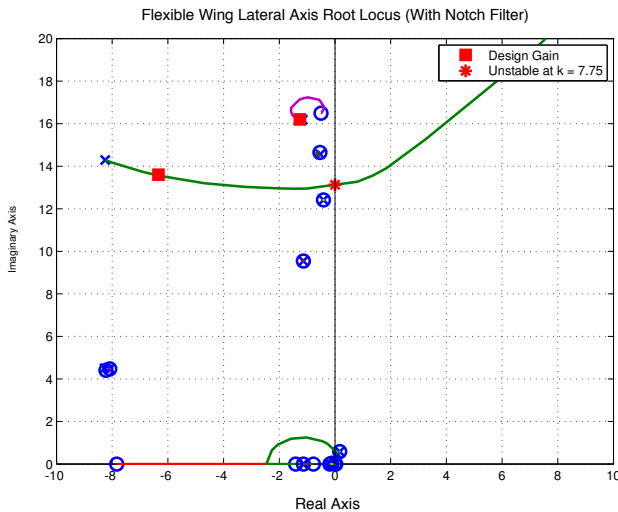


Fig. 36. Root locus plot for roll feedback on the flexible wing model with notch filters

Figures 37 and 38, compare the closed loop roll attitude and yaw rate responses for the various models. The curves in the plots contain the optimized controllers for the Rigid Wing model, the Flex Wing model, and the Flex Wing model with notch filters added. Magnitudes are expressed

in radians for roll attitude commands and rad/sec for yaw rate commands, while the inputs are inches of stick deflection. The yaw response without the notch filters has a large peak around the wing antisymmetric mode frequency (Fig. 38). The notch filter in the feedforward path removes the wing flexibility peaks at the expense of bandwidth reduction. The models all match well at low frequency with differences occurring after 1 rad/sec in both axes.

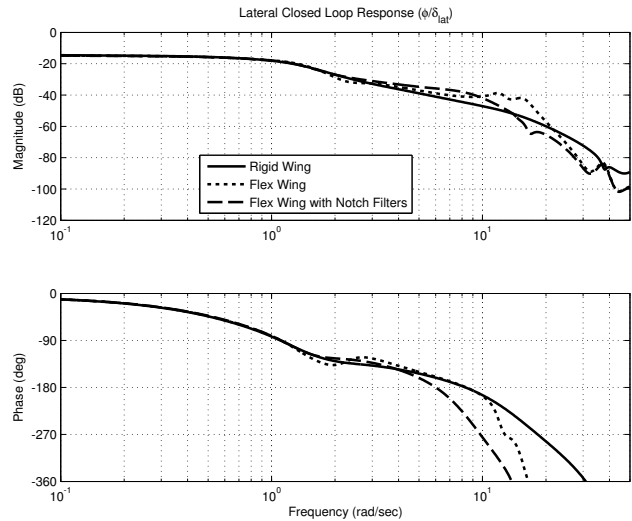


Fig. 37. Closed loop roll attitude command response to pilot lateral stick inputs

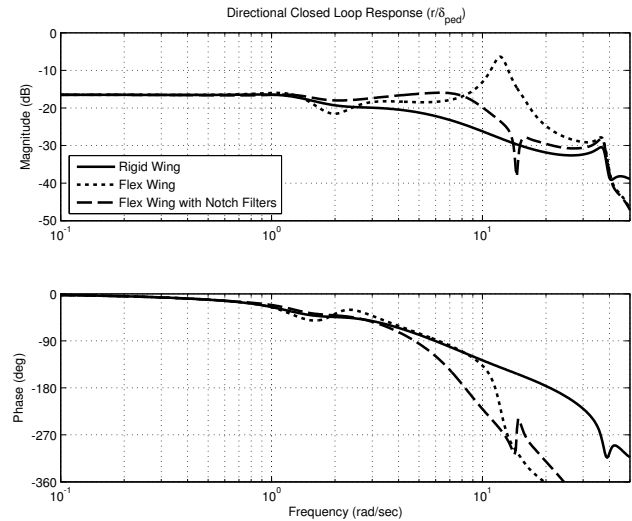


Fig. 38. Closed loop yaw rate command response to pilot pedal inputs.

The higher bandwidth Level 1 region from ADS-33E bandwidth specification in the yaw axis was found to be objectionable to pilots due to the large CG offset of the pilot station, so the roll and yaw attitude bandwidths for the Rigid Wing LCTR were placed within the Level 1 regions of both ADS-33E and the proposed LCTR boundaries from Ref. 8, as shown in Figs. 39 and 40. This was done by hand tuning the natural frequency of the second order roll

axis command model and the time constant of the first order yaw axis model. These same command models were held constant when used for the Flex Wing cases. This was done to see the effect of the flexible wing and notch filters on bandwidth and phase delay. The phase delay of the Rigid Wing model was not achievable in either of the Flex Wing cases, Fig. 39 and 40, meaning a majority of the delay comes from structural flexibility. The notch filters add more phase delay and also reduce the bandwidth when comparing the Flex Wing with Notch Filters to the Flex Wing case. Level 1 handling qualities were achieved for all models in the roll response for both the ADS-33 boundaries as well as the proposed LCTR ones. Level 1 handling qualities were not achievable for the ADS-33E boundaries in yaw for all three models. The bandwidth reduction due to the notch filters places the Flex Wing with Notch Filters model in the Level 2 region of both the ADS-33E boundaries as well as the proposed LCTR boundaries. The Flex Wing case lies in the Level 1 region of the ADS-33E boundaries, but is in the Level 3 region of the proposed LCTR boundaries.

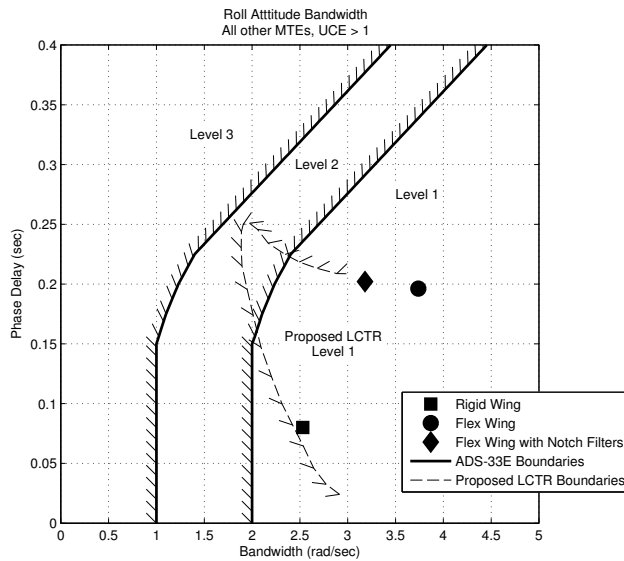


Fig. 39. ADS-33 Roll Bandwidth specification for Hover, all other MTEs

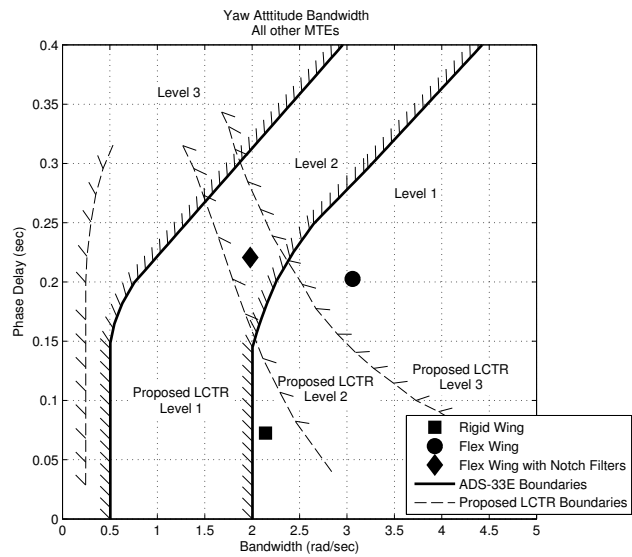


Fig. 40. ADS-33 Yaw Bandwidth specification for Hover, all other MTEs

Time responses to piloted step commands are shown in Figs. 41 and 42. Overall, there is good tracking of roll commands. The yaw rate response shows the excitation of wing modes which are not well damped because there is no active structural damping. The yaw commands produce oscillations of the wing antisymmetric wing mode. The notch filters are able to reduce the oscillation and provide better damped responses. These oscillations are not seen in the roll attitude response because the command model produces a more gradual response, while the yaw model is more aggressive. The rise and settling times for all three yaw responses match well. Again, using the notch filters in the feedforward design was important so that piloted inputs would not excite the wing structural modes, particularly in the yaw axis.

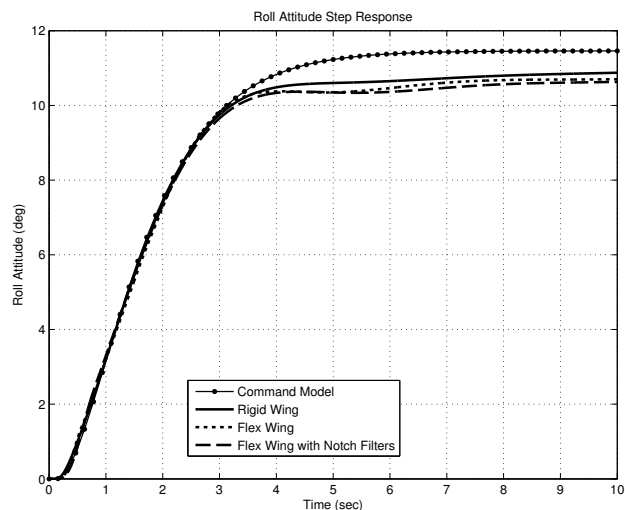


Fig. 41. Closed loop step roll attitude command to pilot lateral stick

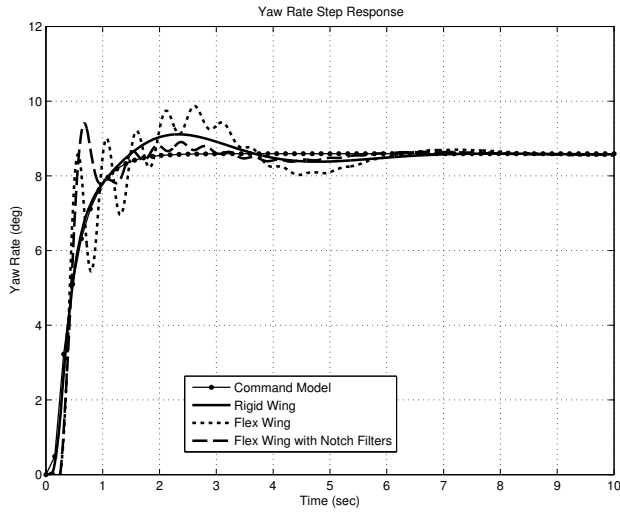


Fig. 42. Closed loop step yaw rate command to pilot pedal inputs

Disturbance rejection plots are shown in Figs. 43 and 44. In the roll axis, the Flex Wing with Notch Filters model regains the disturbance rejection properties of the Rigid Wing model with both the bandwidth and peak response being restored.

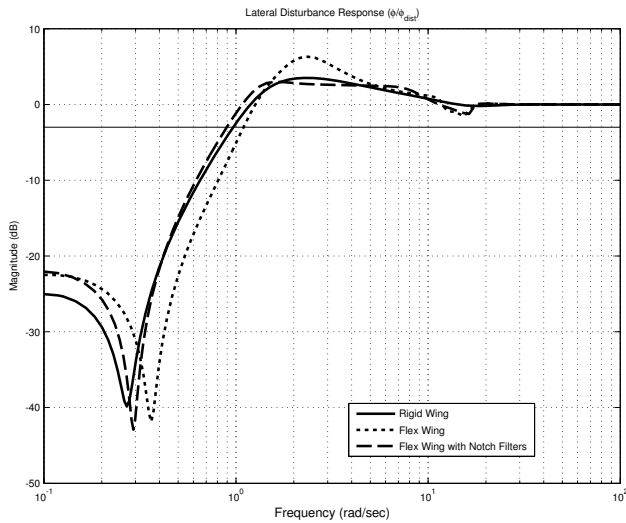


Fig. 43. Roll axis disturbance rejection

The yaw axis disturbance rejection plot shows that the Flex Wing with Notch Filters model has a higher disturbance rejection bandwidth than the flexible wing or rigid wing models. The peak response for the Flex Wing is worse than the other two.

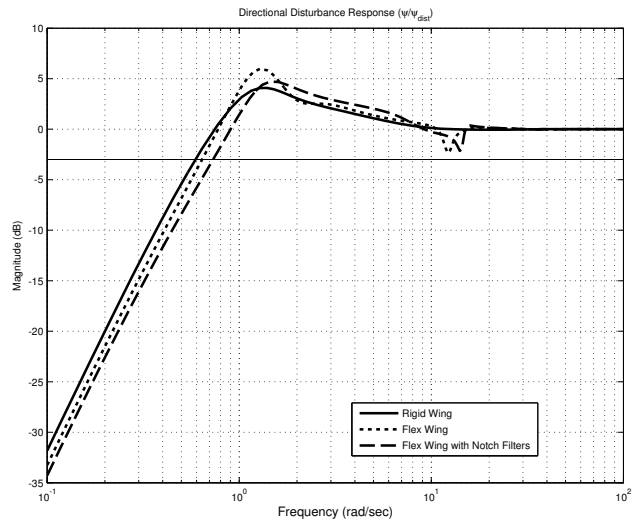


Fig. 44. Yaw axis disturbance rejection

Disturbance rejection properties of the models are compared next in Figs. 45 and 46. Disturbances in roll attitude, $\phi_d = 5$ deg, and yaw attitude, $\psi_d = 5$ deg, were applied for 1 second. In the roll axis, the Flex Wing model has the highest disturbance magnitude peak, given in Table 7 and show in Fig. 43, and thus has the largest response to disturbance as seen in Fig. 45. All three responses in the yaw axis are well damped and take around the same time to settle.

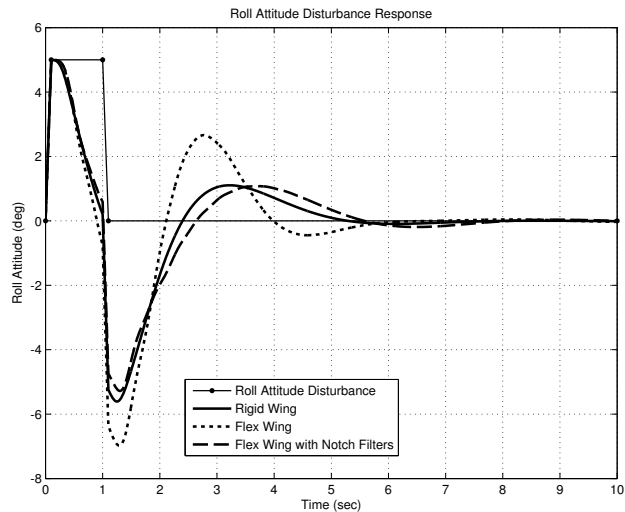


Fig. 45. Closed loop roll attitude response to a 1 second disturbance in roll attitude

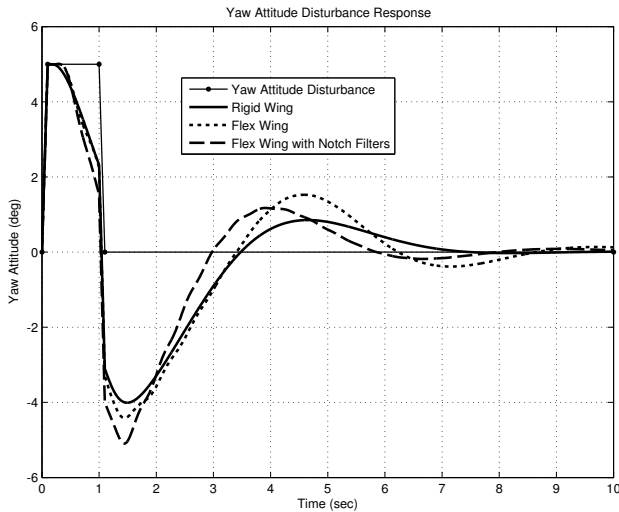


Fig. 46. Closed loop yaw attitude response to a 1 second disturbance in yaw attitude

Discussion

Level 1 stability and handling qualities, with the exception of yaw axis piloted bandwidth, were attained for the Flex Wing with Notch Filters model. The Level 2 ADS-33E bandwidth in the yaw response, Fig. 40, comes from the additional phase lag and bandwidth reduction due to the notch filters. It might be possible to retune the command model to attain Level 1 bandwidth, but all three cases in the current work use the same command model to better demonstrate the effects of flexible wings and notch filters. Care must be given to ensure that the flexible wing mode peak in the magnitude of the broken loop response does not get too close to the 0 dB line, or enter the exclusion zone on the Nichols plot when retuning the command model.

Wing modes were not fed back in the current work. Since wing damping was set to 4%, wing excitation was not directly controllable and structural damping proved to be a bound for some damping specifications. Feeding back wing states or structural load measurements might allow the control system to improve the damping, as well as the stability margins and bandwidth of the flexible wing responses (Ref. 22).

Conclusions

Based on the results shown it can be concluded that:

1. The model correctly predicts behavior when compared to XV-15 flight data in hover and cruise. Differences in the hover responses are attributed to hub modeling. The XV-15 had a gimbaled hub, where the current model has an articulated rotor with hub springs.

2. The LCTR hover configuration shows qualitatively similar dynamics to that of the XV-15. The LCTR HeliUM rigid wing model matches very well the CAMRAD model, which is also rigid.
3. For large aircraft, such as the LCTR, structural and rotor dynamics have large effects in the frequency ranges used for flight control designs.
4. A parallel implementation that decouples rigid-body and structural states retains the majority of the dynamics, reducing modeling complexity and problem size. This implementation also provides a pathway for including structural dynamics in existing rigid body real-time simulation models.
5. Level 1 handling qualities cannot be obtained from a flexible wing aircraft model without notch filters, but the model with the notch filters meets nearly all ADS-33 specifications to Level 1 standards. Notch filters can be used to suppress the structural response but reduce the bandwidth of the system to create a Level 2 aircraft in the yaw axis. Removing the notch filters would give an aircraft with lower phase margin and crossover frequency in this axis. Tests could be conducted to determine if pilots prefer higher bandwidth or improved phase margin and crossover frequency. The notch filters also add phase delay and must be used judiciously to avoid degrading the piloted bandwidth and phase delay too heavily.

References

- ¹Johnson, W., Yamauchi, G., and Watts, M. E., "NASA Heavy Lift Rotorcraft Systems Investigation," NASA/TP-2005-213467, December 2005.
- ²Ferguson, Samuel W., "A Mathematical Model for Real Time Flight Simulation of a Generic Tilt-Rotor Aircraft," NASA CR-166536, Systems Technology, Inc., Mountain View, CA, September 1988
- ³Johnson, W., "A Comprehensive Analytical Model of Rotorcraft Aeromechanics and Dynamics. Part I: Analysis and Development," NASA/TM-81182, June 1980.
- ⁴Acree, C.W., and Johnson, W., "Aeroelastic Stability of the LCTR2 Civil Tiltrotor," AHS Technical Specialist's Meeting, Dallas, TX, October 2008.
- ⁵Acree, C.W., Yeo, H., and Sinsay, J.D., "Performance Optimization of the NASA Large Civil Tiltrotor," NASA/TM-2008-215359, Moffett Field, CA, June 2008
- ⁶Acree, C.W., Tischler, M.B., "Determining XV-15 Aeroelastic Modes from Flight Data with Frequency-Domain Methods" NASA TP-3330, Moffett Field, CA, May 1993.

⁷Blanken, C. L., Lusardi, J.A., Ivler, C.M., Tischler, M.B., Decker, W. A., Malpica, C., Berger, T., Tucker, G.E., Hofinger, M.T., "An Investigation of Rotorcraft Stability - Phase Margin Requirements in Hover," American Helicopter Society 65th Annual Forum, Grapevine, TX, May 2009.

⁸Malpica, C., Decker, W. A., Theodore, C. R., Blanken, C. L., Berger, T., "An Investigation of Large Tilt-Rotor Short-term Attitude Response Handling Qualities Requirements in Hover," American Helicopter Society 66th Annual Forum, Phoenix, AZ, May 2010.

⁹Malpica, C., Theodore, C. R., Decker, W. A., Lawrence, B., and Blanken, C. L., "An Investigation of Large Tilt-Rotor Hover and Low Speed Handling Qualities," American Helicopter Society 67th Annual Forum, Virginia Beach, VA, May 2011.

¹⁰Lawrence, B., Malpica, C., Theodore, C. R., Decker, W. A., and Lindsey, J. E., "Flight Dynamics Aspects of a Large Civil Tiltrotor Simulation using Translational Rate Command," American Helicopter Society 67th Annual Forum, Virginia Beach, VA, May 2011.

¹¹Kim, F.D., Celi, R., Tischler, M.B., "High-Order State Space Simulation Models of Helicopter Flight Mechanics", *Journal of the American Helicopter Society*, Vol. 38, No. 4, October 1993.

¹²Howlett, J.J., "UH-60A Black Hawk Engineering Simulation Program - Volume II - Mathematical Model," NASA CR-166309, Dec. 1981.

¹³Theodore, C. R., "Helicopter Flight Dynamics Simulation with Refined Aerodynamic Modeling," Ph.D. Dissertation, Department of Aerospace Engineering, University of Maryland, College Park, MD, 2000.

¹⁴Amirouche, F.M.L., *Fundamentals of Multibody Dynamics*, Birkhauser, 2006.

¹⁵Tischler, Mark B., "Frequency-Response Identification of XV-15 Tilt-Rotor Aircraft Dynamics", NASA TM-89428. Moffett Field, CA, May 1987.

¹⁶Tischler, Mark B. and Remple, Robert K., *Aircraft and Rotorcraft System Identification: Engineering Methods with Flight Test Examples*, AIAA, 2006.

¹⁷Tischler, Mark B. and Remple, Robert K., *Aircraft and Rotorcraft System Identification: Engineering Methods with Flight Test Examples*, forthcoming, 2012.

¹⁸Chin, A., Brenner, M. J., Pickett, M. D., "Integration of Aeroservoelastic Properties into the NASA Dryden F/A-18 Simulator Using Flight Data from the Active Aeroelastic Wing Program," AIAA Atmospheric Flight Mechanics Conference, Portland, OR, August 2011.

¹⁹Theodore, C.R., Ivler, C.M., Tischler, M.B., Field, E.J., Neville, R.L., Ross, H.P., "System Identification of Large Flexible Transport Aircraft," AIAA Atmospheric Flight Mechanics Conference and Exhibit, Honolulu, HI, August 2008.

²⁰Tischler, M. B., Ivler, C. M., Mansur, M. H., Cheung, K. K., Berger, T., and Berrios, M., "Handling-Qualities Optimization and Trade-offs in Rotorcraft Flight Control Design," Rotorcraft Handling Qualities Conference, University of Liverpool, UK, November 2008.

²¹Anonymous, *Aeronautical Design Standard-33E-PRF, Performance Specification, Handling Qualities Requirements for Military Rotorcraft*, US Army AMCOM, Redstone, AL, March 21, 2000.

²²Dibley, R. P., Allen, M. J., Clarke, R., Gera, J., Hodgkinson, J., "Development and Testing of Control Laws for the Active Aeroelastic Wing Program," NASA TM-2005-213666, Edwards, CA, December 2005.

Appendix A: Kinematics

Positions

The position vector of a point on a body with respect to a reference point can be written as a linear combination of orthogonal unit vectors.

$$x \mathbf{n}_1^j + y \mathbf{n}_2^j + z \mathbf{n}_3^j = [x \ y \ z] \begin{Bmatrix} \mathbf{n}_1^j \\ \mathbf{n}_2^j \\ \mathbf{n}_3^j \end{Bmatrix} = \{\mathbf{q}^j\}^T \{\mathbf{n}^j\} \quad (\text{A.1})$$

$\mathbf{n}_{1,2,3}^j$ are the unit vectors in reference frame j . The formulation allows for arbitrary directions of the unit vectors, but generally they are chosen to be meaningful for a given body. The fuselage unit vectors are those of the standard body axis system, with \mathbf{n}_1 pointing forwards, \mathbf{n}_2 pointing to starboard, and \mathbf{n}_3 pointing down. The starting point for the formulation is an inertial reference frame. This reference frame maintains its orientation in space and so is unaffected by aircraft angular motion. The reference frame always has the z -axis pointing down, with the positive direction of the x and y axes remaining unspecified (but could be prescribed, for example, to point North and East, respectively, if necessary, with no consequences on the results of the present study).

The transformations between reference frames are carried out on the unit vectors using the standard aerospace rotation sequence, i.e., a rotation about the \mathbf{n}_3 axis by angle ψ , followed by a rotation by angle θ about the \mathbf{n}_2^ψ axis resulting from the ψ rotation, and by a rotation by angle ϕ about the \mathbf{n}_1^θ axis resulting from the θ rotation. The transformation matrices between two reference frames j and k are as follows:

$$[\psi] = [S^{1j}] = \begin{bmatrix} \cos \psi & \sin \psi & 0 \\ -\sin \psi & \cos \psi & 0 \\ 0 & 0 & 1 \end{bmatrix}$$

$$[\theta] = [S^{21}] = \begin{bmatrix} \cos \theta & 0 & -\sin \theta \\ 0 & 1 & 0 \\ \sin \theta & 0 & \cos \theta \end{bmatrix}$$

$$[\phi] = [S^{k2}] = \begin{bmatrix} 1 & 0 & 0 \\ 0 & \cos \phi & \sin \phi \\ 0 & -\sin \phi & \cos \phi \end{bmatrix}$$

The intermediate coordinate systems are labeled $\{\mathbf{n}^1\}$ and $\{\mathbf{n}^2\}$.

$$\{\mathbf{n}^1\} = [S^{1j}] \{\mathbf{n}^j\}$$

and

$$\{\mathbf{n}^2\} = [S^{21}] \{\mathbf{n}^1\}$$

The complete transformation from body j to k is:

$$\begin{Bmatrix} \mathbf{n}_1^k \\ \mathbf{n}_2^k \\ \mathbf{n}_3^k \end{Bmatrix} = [\phi] [\theta] [\psi] \begin{Bmatrix} \mathbf{n}_1^j \\ \mathbf{n}_2^j \\ \mathbf{n}_3^j \end{Bmatrix} \quad (\text{A.2})$$

$$= [S^{k2}] [S^{21}] [S^{1j}] \begin{Bmatrix} \mathbf{n}_1^j \\ \mathbf{n}_2^j \\ \mathbf{n}_3^j \end{Bmatrix} \quad (\text{A.3})$$

or more compactly written as:

$$\{\mathbf{n}^k\} = [S^{kj}] \{\mathbf{n}^j\} \quad (\text{A.4})$$

The components of $[S^{kj}]$ are:

$$S^{kj} = \begin{bmatrix} S_{11} & S_{12} & S_{13} \\ S_{21} & S_{22} & S_{23} \\ S_{31} & S_{32} & S_{33} \end{bmatrix} \quad (\text{A.5})$$

where

$$\begin{aligned} S_{11} &= \cos \theta \cos \psi \\ S_{12} &= \cos \theta \sin \psi \\ S_{13} &= -\sin \theta \\ S_{21} &= \sin \phi \sin \theta \cos \psi - \cos \phi \sin \psi \\ S_{22} &= \sin \phi \sin \theta \sin \psi + \cos \phi \cos \psi \\ S_{23} &= \sin \phi \cos \theta \\ S_{31} &= \cos \phi \sin \theta \cos \psi + \sin \phi \sin \psi \\ S_{32} &= \cos \phi \sin \theta \sin \psi - \sin \phi \cos \psi \\ S_{33} &= \cos \phi \cos \theta \end{aligned}$$

For a wing, the unit vectors \mathbf{n}_1 , \mathbf{n}_2 , and \mathbf{n}_3 point, respectively, outwards along the undeformed elastic axis of the wing, forwards towards the leading edge, and upwards. The transformation from the fuselage coordinate system to that of the wing contains wing dihedral and sweep.

Once the transformation matrices from one coordinate system set to another are known, the product of the matrices allows for the formulation of a position vector in any coordinate system. The summing of the displacements in each coordinate system gives the expression for any point in the system. The reference frame is denoted with superscript $(\dots)^0$, and is generally the inertial frame. The superscript increases with each connection. An example for a generic set of connected bodies is given in Fig. A.1. Here, the reference frame is the inertial frame. The segment ζ is an offset from a reference point to the first body and is written in terms of the reference frame. It is set to zero for the present study, but if the bodies are free to move with respect to the reference frame, it could be used to position the bodies with respect to an arbitrary point in the reference frame: for example a location on the ground if the bodies form an aircraft. The position vectors \mathbf{q} locate the connection of

the next body in the current body's coordinate system. The vectors \mathbf{r} locate a point within each body that is not the connection point, a center of mass for example. Thus, the position vector \mathbf{P} , of a point placed by vector \mathbf{r}_3 in the third body relative to a point in the reference frame is found in Eqn. (A.6). This position vector, and the kinematics of the bodies presented, follows the formulation found in Ref. 14. For the tiltrotor of the present study, the bodies are arranged as follows: Body 1 is the aircraft fuselage, Body 2 is the undeformed right wing, and Body 3 is the nacelle. The hub of the opposite rotor is described by a symmetric set of bodies.

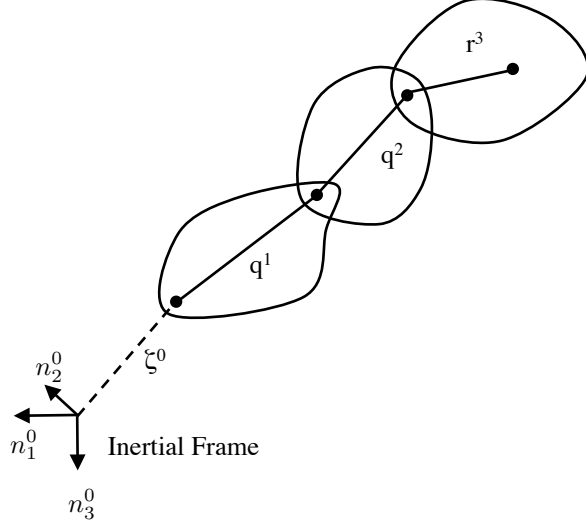


Fig. A.1. Bodies connected together in a multiple body configuration

$$\mathbf{P} = \{\zeta\}^T \{\mathbf{n}^0\} + \{\mathbf{q}^1\}^T \{\mathbf{n}^1\} + \{\mathbf{q}^2\}^T \{\mathbf{n}^2\} + \{\mathbf{r}^3\}^T \{\mathbf{n}^3\} \quad (\text{A.6})$$

We can write a set of unit vectors in the reference frame for the tilt rotor as follows:

$$\{\mathbf{n}^3\} = [S^{32}] [S^{21}] [S^{10}] \{\mathbf{n}^0\} = [S^{30}] \{\mathbf{n}^0\} \quad (\text{A.7})$$

and thus:

$$\mathbf{P} = \left(\{\zeta\}^T + \{\mathbf{q}^1\}^T [S^{10}] + \{\mathbf{q}^2\}^T [S^{20}] + \{\mathbf{r}^3\}^T [S^{30}] \right) \{\mathbf{n}^0\} \quad (\text{A.8})$$

or more generally as:

$$\mathbf{P} = \left(\{\zeta\}^T + \sum_{i=1}^{n-1} \{\mathbf{q}^i\}^T [S^{i0}] + \{\mathbf{r}^n\}^T [S^{n0}] \right) \{\mathbf{n}^0\} \quad (\text{A.9})$$

Flexibility effects show up by modifying the transformation matrices $[S^{kj}]$ to include the rotations due to structural flexibility, as well as adding displacements. A constant wing deflection will alter the connection point of the

nacelle since the wing coordinate system is in the undeformed frame. The deflection will also introduce additional rotations in the transformation from the wing undeformed coordinate system to the nacelle coordinate system. Displacements and rotations at the connection are functions of the modal temporal coordinates, $\rho(t)$ and the spatial components of the finite element beam model, $[\mathbf{N}(x)]$. Since the beam finite element model has position and slopes at each node, flexible displacements and rotations can be written as:

$$\begin{Bmatrix} \mathbf{q}_f \\ \alpha_f \end{Bmatrix} = [\mathbf{N}(x)] \rho(t) \quad (\text{A.10})$$

Here, \mathbf{q}_f is the connection point's displacement due to flexibility, and α_f is the rotation at that point. The displacement for the connection point, including flexibility contributions for the next body is then:

$$\bar{\mathbf{q}}^j = \mathbf{q}^j + \mathbf{q}_f^j \quad (\text{A.11})$$

The beam element formulation assumes rotations in the same order as the coordinate system transformations. Therefore, the transformation to the coordinate system of body upstream of the flexible body, when written in the same form as Eqn. (A.4), contains an additional set of rotations due to flexibility:

$$\{\mathbf{n}^k\} = \underbrace{[S^{kf}]}_{[S^{kj}]} [S^{fj}] \{\mathbf{n}^j\} \quad (\text{A.12})$$

where,

$$[S^{fj}] = [\phi_f] [\theta_f] [\psi_f] \quad (\text{A.13})$$

and ϕ_f, θ_f , and ψ_f are components of α_f , from Eqn. (A.10). The matrix $[S^{kf}]$ now has the same form as Eqn. (A.2), and is the transformation from the connection point coordinate system, which is now the deformed coordinate system, to the coordinate system of the next body. In the equation above, and following the example of the flexible wing, superscript j denotes the wing undeformed coordinate system, while superscript k denotes the nacelle coordinate system. This matrix takes into account the static wing deformation.

The full position vector of any point on the aircraft, including flexibility contributions is now:

$$\mathbf{P} = \left(\{\zeta\}^T + \sum_{i=1}^{n-1} \{\bar{\mathbf{q}}^i\}^T [S^{i0}] + \{\mathbf{r}^n\}^T [S^{n0}] \right) \{\mathbf{n}^0\} \quad (\text{A.14})$$

Velocities

Once the position vector of the point is known, the velocity and acceleration vectors follow. The velocity vector is

simply the time derivative of the position vector.

$$\mathbf{v} = \frac{d\mathbf{P}}{dt} = \left(\left\{ \dot{\boldsymbol{\zeta}} \right\}^T + \sum_{i=1}^{n-1} \left(\left\{ \dot{\mathbf{q}}^i \right\}^T [S^{i0}] + \left\{ \dot{\mathbf{q}}^i \right\}^T [\dot{S}^{i0}] \right) + \left\{ \dot{\mathbf{r}}^n \right\}^T [S^{n0}] + \left\{ \dot{\mathbf{r}}^n \right\}^T [\dot{S}^{n0}] \right) \left\{ \mathbf{n}^0 \right\} \quad (\text{A.15})$$

Here, $\dot{\boldsymbol{\zeta}}$ is the velocity of the aircraft CG in the inertial reference frame. The time derivatives of the transformation matrices, $[\dot{S}^{i0}]$, as well as $\dot{\mathbf{q}}^i$ and $\dot{\mathbf{r}}^n$ take into account motion due to flexibility. The position and angular time derivatives again come from the beam finite element:

$$\begin{Bmatrix} \dot{\mathbf{q}}_f \\ \boldsymbol{\omega}_f \end{Bmatrix} = [\mathbf{N}(x)] \dot{\boldsymbol{\rho}}(t) \quad (\text{A.16})$$

Since the bodies are not allowed to translate with respect to each other, the velocity contribution, $\dot{\mathbf{q}}$ only has terms associated with flexibility. In keeping the notation from Eqn. (A.11):

$$\dot{\mathbf{q}}^j = \mathbf{0} + \dot{\mathbf{q}}_f^j = \dot{\mathbf{q}}_f^j \quad (\text{A.17})$$

The time derivatives of the transformation matrices require more development. The flexible contributions to angular rates, $\boldsymbol{\omega}_f$ have the form:

$$\begin{aligned} \boldsymbol{\omega}_f &= \psi \mathbf{n}_3^j + \dot{\theta} \mathbf{n}_2^j + \dot{\phi} \mathbf{n}_1^j \\ &= (\dot{\phi} \cos \theta \cos \psi - \dot{\theta} \sin \psi) \mathbf{n}_1^j + \\ &\quad (\dot{\phi} \cos \theta \sin \psi + \dot{\theta} \cos \psi) \mathbf{n}_2^j + (\psi - \phi \sin \theta) \mathbf{n}_3^j \end{aligned} \quad (\text{A.18})$$

$$\quad (\text{A.19})$$

Notice the unit vectors in the final equation above are in the ‘‘downstream’’ coordinate system, i.e., the coordinate system of the next body proceeding from the end of the tree toward the beginning. For the wing, or any flexible body, this is the coordinate system before elastic deformation. These angular rates act on the upstream body to the flexible body, for the tilt-rotor example, the nacelle. In general, the formulation presented assigns rotation rates in the coordinate system of the rotating body, as opposed to the upstream body. Before they are converted to the nacelle coordinate system, they must be converted through the wing deformed coordinate system as in Eq. (A.12). This allows for easier manipulation of the $[\dot{S}]$ matrices later on.

$$\left\{ \boldsymbol{\omega}_f^j \right\}^T \left\{ \mathbf{n} \right\}^j = \underbrace{\left\{ \boldsymbol{\omega}_f^j \right\}^T}_{\boldsymbol{\omega}_f^k} \left[S^{jk} \right] \left\{ \mathbf{n} \right\}^k \quad (\text{A.20})$$

Note the superscript order of matrix $[S^{jk}]$. For a rigid aircraft, Eq. (A.18) gives the Euler rates at the CG in the coordinate systems local to each Euler rate. For example, $\dot{\theta}$ is the Euler rate after a transformation by ψ has occurred. Equation (A.19) gives the Euler rates in the inertial coordinate system, and Eq. (A.20) transforms the Euler rates into

the body axis. The Euler rates in the body axis give the standard flight dynamics formulation of roll, pitch, and yaw rates.

Since the transformation matrices are pure rotations, their inverse is equal to their transpose:

$$[S^{kj}] = [S^{jk}]^T = [S^{jk}]^{-1} \quad (\text{A.21})$$

Taking the time derivative of Eqn. A.4 directly, we obtain:

$$[\dot{S}^{kj}] = [\Omega^{kj}] [S^{kj}] \quad (\text{A.22})$$

where $[\Omega]$ is a skew symmetric matrix. using $\boldsymbol{\omega}_f^k$ from Eqn. (A.20):

$$[\Omega^{kj}] = \begin{bmatrix} 0 & \boldsymbol{\omega}_{3f}^k & -\boldsymbol{\omega}_{2f}^k \\ -\boldsymbol{\omega}_{3f}^k & 0 & \boldsymbol{\omega}_{1f}^k \\ \boldsymbol{\omega}_{2f}^k & -\boldsymbol{\omega}_{1f}^k & 0 \end{bmatrix} \quad (\text{A.23})$$

The formulation for $[\dot{S}]$ thus far only accounts for a single coordinate transformation, so for two tangent bodies. For groups of transformations, as is the case with almost any multibody configuration, the treatment of $[\dot{S}]$ has additional components.

$$[S^{n0}] = [S^{n,n-1}] [S^{n-1,n-2}] \dots [S^{21}] [S^{10}] \quad (\text{A.24})$$

taking the time derivative:

$$\begin{aligned} \frac{d}{dt} [S^{n0}] &= \frac{d}{dt} ([S^{n,n-1}] [S^{n-1,n-2}] \dots [S^{21}] [S^{10}]) \quad (\text{A.25}) \\ [\dot{S}^{n0}] &= ([\dot{S}^{n,n-1}] [S^{n-1,n-2}] \dots [S^{21}] [S^{10}]) + \\ &\quad ([S^{n,n-1}] [\dot{S}^{n-1,n-2}] \dots [S^{21}] [S^{10}]) + \dots \\ &\quad ([\dot{S}^{n,n-1}] [S^{n-1,n-2}] \dots [\dot{S}^{21}] [S^{10}]) + \\ &\quad ([\dot{S}^{n,n-1}] [S^{n-1,n-2}] \dots [S^{21}] [\dot{S}^{10}]) \end{aligned} \quad (\text{A.26})$$

Each individual $[\dot{S}^{k,k-1}]$ is formulated in the same fashion as Eqn. (A.22). The trigonometry of Eqn. (A.26) does not need to be carried out each time. Note the following treatment of $[\dot{S}^{n0}]$.

$$\begin{aligned} [\dot{S}^{10}] &= [\Omega^{10}] [S^{10}] \\ [\dot{S}^{20}] &= [\dot{S}^{21}] [S^{10}] + [S^{21}] [\dot{S}^{10}] \\ &= [\Omega^{21}] [S^{20}] + [S^{21}] [\Omega^{10}] [S^{10}] \\ &= [\Omega^{21}] [S^{20}] + [S^{21}] [\dot{S}^{10}] \\ &\dots \\ [\dot{S}^{n0}] &= [\Omega^{n,n-1}] [S^{n0}] + [S^{n,n-1}] [\dot{S}^{n-1,0}] \\ [\dot{S}^{n0}] &= [\Omega^{n0}] [S^{n0}] \end{aligned} \quad (\text{A.27})$$

In general, $[\dot{S}^{n0}]$ is built from outwards starting from the reference frame as each body’s angular velocity has contributions from all time derivatives between bodies 0 and n , and is in the reference coordinate system. The velocity of a

component of the multibody system can now be expressed using Eqn. (A.15). Often times the angular velocities of a body in the local coordinate system need to be used. This is easily done using Eqn. (A.27). Using the formulation of Eqn. (A.22), and Eqn. (A.23):

$$[\Omega^{kj}] = [\dot{S}^{kj}] [S^{kj}]^{-1} = [\dot{S}^{kj}] [S^{kj}]^T \quad (\text{A.28})$$

The skew-symmetric matrix gives the angular velocities of body k in the coordinate system of body k so individual angular rates can readily be extracted from its components. If the rates are desired in a different coordinate system they can be transformed using Eqn. (A.20).

Accelerations

The linear and angular acceleration vectors are derived in much the same way as the velocity vectors. Taking an additional time derivative of Eqn. (A.15):

$$\begin{aligned} \mathbf{a} = \frac{d\mathbf{v}}{dt} = & \left(\{ \ddot{\zeta} \}^T + \sum_{i=1}^{n-1} \left(\{ \ddot{q}^i \}^T [S^{i0}] + 2 \{ \dot{q}^i \}^T [\dot{S}^{i0}] + \right. \right. \\ & \left. \left. \{ \ddot{q}^i \}^T [\dot{S}^{i0}] \right) + \{ \ddot{r}^n \}^T [S^{n0}] + 2 \{ \dot{r}^n \}^T [\dot{S}^{n0}] + \right. \\ & \left. \{ \ddot{r}^n \}^T [\dot{S}^{n0}] \right) \{ n^0 \} \end{aligned} \quad (\text{A.29})$$

The first term in the derivative is the linear acceleration of the aircraft in the inertial reference frame. \ddot{q}^T terms are linear accelerations of the bodies with respect to one another. The tilt-rotor model does allow for linear motion of aircraft components next to each other. Much like the velocity component in Eqn. (A.17), this terms only contains accelerations due to flexibility. The second time derivative of the transformation matrix $[\dot{S}^{i0}]$ is the remaining component that has not been derived yet. To determine $[\dot{S}^{i0}]$, one could take time derivatives of the transformation matrices one by one, as in Eqn. (A.26). Since $[\Omega^{i0}]$, is readily available, as in Eqn. (A.27), the following treatment is much abbreviated.

$$\frac{d}{dt} [S^{i0}] = \frac{d}{dt} ([\Omega^{n0}] [S^{n0}]) \quad (\text{A.30})$$

$$\begin{aligned} &= [\dot{\Omega}^{n0}] [S^{n0}] + [\Omega^{n0}] [\dot{S}^{n0}] \\ [\dot{S}^{n0}] &= [\dot{\Omega}^{n0}] [S^{n0}] + [\Omega^{n0}] [\Omega^{n0}] [S^{n0}] \end{aligned} \quad (\text{A.31})$$

Here $[\dot{\Omega}^{n0}]$ is a skew symmetric matrix containing the summed angular accelerations of bodies 0 to n in the final body's coordinate system. It is derived in the same fashion as the skew symmetric matrix of angular velocities, Eqn. (A.23), which comes from the sequence of rotations given by Eqn. (A.18).